Numerical Model Reduction of Multi-Scale Electrochemical Ion Transport

International Journal for Numerical Methods in Engineering

WILEY

RESEARCH ARTICLE OPEN ACCESS

Numerical Model Reduction of Multi-Scale Electrochemical Ion Transport

Vinh Tu[1,2] | Fredrik Larsson[1] | Kenneth Runesson[1] | Ralf Jänicke[2]

[1]Department of Industrial and Materials Science, Chalmers University of Technology, Gothenburg, Sweden | [2]Institute of Applied Mechanics, Technische Universität Braunschweig, Braunschweig, Germany

Correspondence: Vinh Tu (vinh.tu@chalmers.se)

Received: 21 October 2025 | **Revised:** 20 February 2026 | **Accepted:** 4 March 2026

Keywords: computational homogenization | Numerical Model Reduction | snapshot POD | transient electrochemical transport

ABSTRACT

In this paper, we develop a Numerical Model Reduction (NMR) framework for multi-scale modeling of electro-chemically coupled ion transport. Upon introducing the governing equations and employing Variationally Consistent Homogenization, a two-scale model, consisting of a macro-scale and a sub-scale part, is obtained. Instead of solving for the computationally expensive FE^2 simulation, where the macro-scale and sub-scale problems are solved in a nested fashion, we exploit NMR by training a surrogate model that replaces the sub-scale finite element simulations. The surrogate model is trained by performing Proper Orthogonal Decomposition on snapshots of the primary fields. Each macro-scale quadrature point is no longer occupied by a Representative Volume Element simulation; instead, it is replaced by a surrogate model that consists of a system of Ordinary Differential Equations. In this way, a computationally efficient solution scheme for solving two-scale problems is obtained.

1 | Introduction

The focus of the paper is on efficient modeling of electrochemical ion transport in biphasic microstructures, e.g., microstructures with distinct solid and liquid phases. An example of such a material is the Structural Battery Electrolyte (SBE) [1–4], which is an essential component to the structural battery [5]. Unlike conventional monofunctional batteries, structural batteries are multifunctional; they can simultaneously store and deliver energy while carrying mechanical loads. In contrast to conventional batteries that use liquid electrolytes for ion transport, structural batteries employ a Structural Battery Electrolyte (SBE), which is tailored for both ionic conductivity and mechanical integrity [6]. The SBE is biphasic in the sense that it consists of a nanoporous polymer phase that is filled with liquid electrolyte. Here, the role of the liquid electrolyte is to allow for ion transfer, while the solid polymer phase contributes to the mechanical properties. In the present paper, we will develop a framework for efficient simulation of electrochemical ion transport, using the SBE as the primary application example.

Numerous studies in the literature focus on the modeling and simulation of electrochemical systems. Notably, Newman and colleagues developed numerical models for coupled electrochemical reaction-diffusion processes in batteries [7–9].

Regarding ion transport modeling in conventional batteries, significant contributions include the works of Samson et al. [10], Danilov and Notten [11], Dickinson et al. [12], and Bauer et al. [13]. On the other hand, employing multi-scale methods to account for micro-heterogeneities in the microstructure of electrochemical systems is a less explored area.

Starting with (classical first-order) computational homogenization [14, 15] of coupled problems; Özdemir et al. [16] extended the computational homogenization technique towards fully coupled thermo-mechanical analysis. Similarly, Schröder and Keip [17] treat the electro-mechanically coupled boundary value problem using computational homogenization. Noteworthy is the work of Javili et al. [18], which considers computational homogenization in magneto-mechanics. For applications of computational homogenization towards electrochemical systems (i.e., the focus of the present paper), we note the works of Salvadori et al. [19–21] and Tu et al. [22]. However, simulations based on computational homogenization tend to become computationally inefficient to solve as the complexity of the problem increases, especially in 3D.

A viable strategy to reduce the cost of solving two-scale problems is to exploit Numerical Model Reduction (NMR).[1] One of the earliest studies on NMR in the context of computational homogenization methods was conducted by Fish and co-workers [23]. They proposed "eigendeformation-based-reduced-order homogenization," which follows along the lines of Transformation Field Analysis (TFA). This theory was originally proposed by Dvorak and Benveniste [24, 25]; it allowed for a reduction of macroscopic internal variables, but only under the assumption of piecewise uniform microscopic fields of internal variables. Consequently, the more general theory of Nonuniform Transformation Field Analysis (NTFA) was developed by Michel and Suquet [26]. They introduced the notion of tensorial plastic modes that allow for deviations from uniformity, as opposed to the scalar plastic modes from TFA.

One of the most powerful tools in the context of model order reduction of space- and time-dependent data is the Proper Orthogonal Decomposition (POD). This method exploits a separation of variables, resulting in a decomposition consisting of spatial modes. More precisely, POD results in a decomposition of the snapshot data into spatial modes. The strategy of accelerating two-scale simulations based on POD has been treated by Yvonnet et al. [27, 28] and Guo et al. [29]. The theory of NTFA has been integrated with POD by Rousette et al. [30] and Fritzen et al. [31, 32] for viscoelastic and standard dissipative materials. More recently, NMR has been explored in the context of computational homogenization of porous media by Jänicke et al. [33, 34] and Ekre et al. [35].

In this paper, the goal is to develop an NMR framework using snapshot POD for multi-scale modeling of electrochemical ion transport. The balance equations of the problem are Gauss's law coupled with a conservation law for each mobile species. Variationally Consistent Homogenization (VCH) [36] is used to establish a two-scale model, i.e., a smooth macro-scale problem and a sub-scale problem. The two-scale problem can be solved via the Finite Element squared (FE^2) method, which is a solution scheme that solves both problems in a nested fashion. As previously mentioned, such a solution scheme can become computationally expensive. Therefore, it is appealing to exploit NMR by training a surrogate model that replaces the sub-scale finite element simulations. Here, the surrogate model is trained by accumulating POD modes from snapshot data that are used to approximate the primary solution fields. Hence, the RVE sub-scale problem no longer needs to be solved in each macro-scale quadrature point; instead, it is replaced by the surrogate model, which corresponds to a system of upscaled Ordinary Differential Equations (ODE). This leads to a computationally efficient solution scheme for solving two-scale problems.

The remainder of the paper is structured as follows: Governing equations are briefly established for the fine-scale problem in Section 2. Based on the fine-scale model, the corresponding two-scale problem is deduced via VCH in Section 3. Snapshot POD-based NMR is presented in Section 4. Finally, the paper concludes with computational results in Section 5 and a discussion in Section 6.

2 | Governing Equations

The governing equations for electrochemical ion transport are briefly described in this section, while the relevant constitutive relations are defined shortly after. The current electrochemical system of interest corresponds to a biphasic material consisting of an electrolyte domain Ω_E and a solid polymer domain Ω_S not containing mobile ions, see Figure 1. All ion-related equations are formulated in a general format for any number of ions $\alpha = 1, 2, \dots, N$, but the electrochemical system considered in the numerical simulations will consist of a mobile ion, e.g., Li^+, and a corresponding companion anion (e.g., PF_6^-). For brevity, we use the abbreviation X^- for the anion.

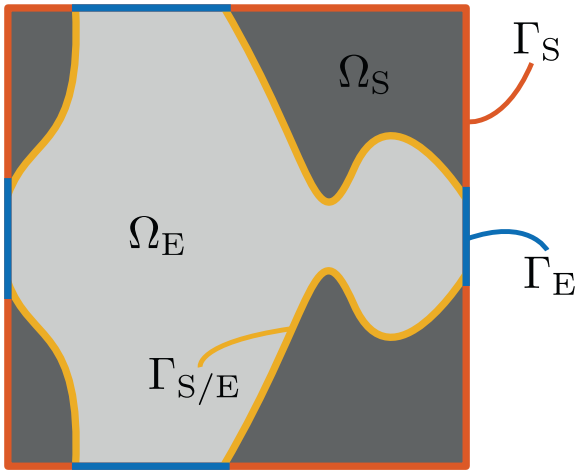

FIGURE 1 | The SBE consists of solid and liquid electrolyte domains, $\Omega = \Omega_S \cup \Omega_E$. The whole outer boundary of the SBE is decomposed as $\partial\Omega = \Gamma_S \cup \Gamma_E = \Gamma_D^{(\varphi)} \cup \Gamma_N^{(\varphi)}$, and the boundary surrounding the liquid electrolyte domain is decomposed as $\partial\Omega_E = \Gamma_E \cup \Gamma_{S/E} = \Gamma_{D,\alpha}^{(\mu)} \cup \Gamma_{N,\alpha}^{(\mu)} \cup \Gamma_{S/E}$.

2.1 | Balance Equations for the Fine-Scale Problem

Restricting to electro-statics, find the electric potential $\varphi(\boldsymbol{x}, t) : \Omega \times \mathbb{R}^+ \to \mathbb{R}$ and the chemical potentials $\mu_\alpha(\boldsymbol{x}, t) : \Omega_E \times \mathbb{R}^+ \to \mathbb{R}$, $\alpha = 1, 2, \ldots, N$, that solve the system

$$\rho - \boldsymbol{d} \cdot \boldsymbol{\nabla} = 0 \qquad \text{in } \Omega \times (0, T], \tag{1a}$$

$$\partial_t c_\alpha + \boldsymbol{j}_\alpha \cdot \boldsymbol{\nabla} = 0 \qquad \text{in } \Omega_E \times (0, T], \tag{1b}$$

with boundary conditions

$$\varphi = \varphi^p \qquad \text{on } \Gamma_D^{(\varphi)} \times (0, T], \tag{2a}$$

$$d := \boldsymbol{d} \cdot \boldsymbol{n} = d^p \qquad \text{on } \Gamma_N^{(\varphi)} \times (0, T], \tag{2b}$$

$$\mu_\alpha = \mu_\alpha^p \qquad \text{on } \Gamma_{D,\alpha}^{(\mu)} \times (0, T], \tag{2c}$$

$$j_\alpha := \boldsymbol{j}_\alpha \cdot \boldsymbol{n} = j_\alpha^p \qquad \text{on } \Gamma_{N,\alpha}^{(\mu)} \times (0, T], \tag{2d}$$

$$j_\alpha = 0 \qquad \text{on } \Gamma_{S/E} \times (0, T], \tag{2e}$$

and initial conditions

$$c_\alpha(\bullet, 0) = c_{\alpha,0} \quad \text{in } \Omega_E. \tag{3}$$

The strong form of the problem is completed with the constitutive relations defined in the subsequent section. Once again, see Figure 1 for the domain and boundary decompositions.

Gauss' law is used in Equation (1a) to resolve the electric potential, where ρ and $\boldsymbol{d}$ are the free charge density per unit volume and the electric flux density (electric displacement field), respectively. The equation is valid on the entire domain $\Omega = \Omega_S \cup \Omega_E$ and the boundary conditions are exemplified on $\partial\Omega = \Gamma_D^{(\varphi)} \cup \Gamma_N^{(\varphi)}$ in terms of Dirichlet (2a) and Neumann conditions (2b).

The chemical potential is solved for using Equation (1b), which expresses the conservation of species α in terms of the volume specific molar concentration c_α and the molar (ionic) flux $\boldsymbol{j}_\alpha$. This equation is valid only in the liquid electrolyte domain Ω_E, where the boundary is decomposed as $\partial\Omega_E = \Gamma_{D,\alpha}^{(\mu)} \cup \Gamma_{N,\alpha}^{(\mu)} \cup \Gamma_{S/E}$. Here, we further decompose the external boundary $\Gamma_E = \Gamma_{D,\alpha}^{(\mu)} \cup \Gamma_{N,\alpha}^{(\mu)}$ to exemplify Dirichlet and Neumann boundary conditions in Equations (2c) and (2d). This means that the ionic transport processes inside the solid domain Ω_s are neglected. Additionally, Equation (2e) is used to prohibit ion transport through the solid-electrolyte interface $\Gamma_{S/E} = \partial\Omega_S \cap \partial\Omega_E$.

A more detailed discussion of the introduced equations is provided in Reference [37].

2.2 | Constitutive Relations of the Fine-Scale Model

The electric flux density $\boldsymbol{d}$ and the ionic flux $\boldsymbol{j}_\alpha$ are defined as

$$\boldsymbol{d} := \boldsymbol{\epsilon} \cdot \boldsymbol{E}, \quad \boldsymbol{E}[\varphi] := -\boldsymbol{\nabla}\varphi, \tag{4a}$$

$$\boldsymbol{j}_\alpha := -\boldsymbol{M}_\alpha \cdot [\boldsymbol{\nabla}\mu_\alpha + z'_\alpha \boldsymbol{\nabla}\varphi], \tag{4b}$$

where $z'_\alpha = F z_\alpha$ corresponds to the ionic charge of mobile species α. Here, F is the Faraday constant and z_α is the valency of species α. The material properties are given as the electric permittivity $\boldsymbol{\epsilon}$ and the ionic mobility $\boldsymbol{M}_\alpha$ of species α. Both quantities are second-rank tensors that can, in the simple case of material isotropy, be condensed to the scalar electric permittivity ϵ and the scalar ionic mobility M_α.

Furthermore, the charge density ρ (charge per unit volume) and the molar concentration c_α (mol per unit volume) of species α are defined as

$$\rho := \begin{cases} \sum_{\alpha=1}^{N} z'_\alpha c_\alpha & \text{in } \Omega_{\mathrm{E}}, \\ 0 & \text{in } \Omega_{\mathrm{S}}, \end{cases} \tag{5a}$$

$$c_\alpha := c_\alpha(\{\mu_\beta\}_{\beta=1}^{N}) \qquad \text{in } \Omega_{\mathrm{E}}. \tag{5b}$$

Under the assumption that we have a dilute (typically molalities below 0.001 mol/kg [38]) distribution of charged ions in the electrolyte, then we model the relation between chemical potential and concentration as follows: $\mu_\alpha = \mu_{\alpha,0} + RT \ln\left(\gamma_\alpha(c_\alpha)\, c_\alpha\right)$, where $\mu_{\alpha,0}$ is the reference chemical potential of species α, and $\gamma_\alpha = \gamma_\alpha(c_\alpha)$ is the activity coefficient of species α. Here, we have made the assumption that the concentration of an ion depends solely on the chemical potential of the same ion.

Further, if the chemical potential changes are small around the concentration level $c_\alpha = c_{\alpha,0}$, then a linearization is possible. Linearization gives

$$c_\alpha = k_\alpha \mu_\alpha + c_{\alpha,0}. \tag{6}$$

Here, k_α depends on the choice of $\gamma_\alpha(c_\alpha)$. In the subsequent analysis, we choose γ_α constant, which results in $k_\alpha = \frac{c_{\alpha,0}}{RT}$.

Finally, the current density in the electrochemical system can be computed via Faraday's rule of electrolysis as

$$\boldsymbol{i} := \sum_{\alpha=1}^{N} z'_\alpha \boldsymbol{j}_\alpha. \tag{7}$$

2.3 | Weak Format of the Fine-Scale Problem

The standard space-variational format corresponding to (1) reads: Find (φ, μ_α) in the appropriately defined spaces $\mathbb{P} \times \{\mathbb{M}_\alpha\}_{\alpha=1}^{N}$ that solve

$$\int_\Omega \delta\varphi\ \rho\ \mathrm{d}\Omega + \int_\Omega \boldsymbol{\nabla}\delta\varphi \cdot \boldsymbol{d}\ \mathrm{d}\Omega = \int_{\Gamma_{\mathrm{N}}^{(\varphi)}} \delta\varphi\ d^{\mathrm{p}}\ \mathrm{d}\Gamma \qquad \forall \delta\varphi \in \mathbb{P}^0, \tag{8a}$$

$$\int_{\Omega_{\mathrm{E}}} \delta\mu_\alpha\ \partial_{\mathrm{t}} c_\alpha\ \mathrm{d}\Omega - \int_{\Omega_{\mathrm{E}}} \boldsymbol{\nabla}\delta\mu_\alpha \cdot \boldsymbol{j}_\alpha\ \mathrm{d}\Omega = -\int_{\Gamma_{\mathrm{N}}^{(\alpha)}} \delta\mu_\alpha\ j_\alpha^{\mathrm{p}}\ \mathrm{d}\Gamma \quad \forall \delta\mu_\alpha \in \mathbb{M}_\alpha^0, \tag{8b}$$

$\alpha = 1, 2, \ldots, N$, where $\mathbb{P}^0$ and $\{\mathbb{M}_\alpha^0\}_{\alpha=1}^{N}$ are the appropriately defined test spaces. Initial conditions are appropriately defined.

3 | Two-Scale Model of Electrochemical Ion Transport

When the microstructure features are small relative to the size of the computational domain, then it becomes computationally infeasible to solve the fully resolved single-scale problem that contains both scales. However, the computational cost can be reduced by employing computational homogenization, which is a two-scale modeling approach that results in a smooth macro-scale problem and a sub-scale RVE problem. The classical homogenization method uses the Hill-Mandel condition to constrain the virtual work of the RVE to be equal to the virtual work at the corresponding macroscopic material point. A natural extension of the Hill Mandel condition for transient problems is to link the virtual power instead [33, 39]. However, in this paper, we do this by exploiting the VCH framework to generalize the Hill Mandel condition and to deduce the two-scale model. In other words, the Hill-Mandel condition is built in by construction in VCH [36].

The main steps of VCH consist of the following:

i. Define the RVE volume averaging operators and the porosity as

$$\langle \bullet \rangle_{\square} := \frac{1}{|\Omega_{\square}|} \int_{\Omega_{\square}} \bullet \, \mathrm{d}\Omega, \tag{9a}$$

$$\langle \bullet \rangle_{\square,\mathrm{E}} := \frac{1}{|\Omega_{\square,\mathrm{E}}|} \int_{\Omega_{\square,\mathrm{E}}} \bullet \, \mathrm{d}\Omega, \tag{9b}$$

$$\phi := \frac{|\Omega_{\square,\mathrm{E}}|}{|\Omega_{\square}|}, \tag{9c}$$

and surface averaging operators as

$$\langle\langle \bullet \rangle\rangle_{\square} := \frac{1}{|\Omega_{\square}|} \int_{\Gamma_{\square^+}} \bullet \, \mathrm{d}\Gamma, \tag{10a}$$

$$\langle\langle \bullet \rangle\rangle_{\square,\mathrm{E}} := \frac{1}{|\Omega_{\square,\mathrm{E}}|} \int_{\Gamma_{\square^+,\mathrm{E}}} \bullet \, \mathrm{d}\Gamma. \tag{10b}$$

ii. Apply the running average approximation as follows

$$\int_{\Omega} \bullet \, \mathrm{d}\Omega \approx \int_{\Omega} \langle \bullet \rangle_{\square} \, \mathrm{d}\Omega, \tag{11}$$

$$\int_{\Omega_{\mathrm{E}}} \bullet \, \mathrm{d}\Omega \approx \int_{\Omega} \phi \langle \bullet \rangle_{\square,\mathrm{E}} \, \mathrm{d}\Omega, \tag{12}$$

i.e., every integrand in the weak format of the fine-scale problem is replaced by the volume-averaged counterpart.

iii. Assume first-order homogenization as follows

$$\varphi = \varphi^{\mathrm{M}}[\overline{\varphi}] + \varphi^{\mathrm{S}}, \tag{13a}$$

$$\mu_{\alpha} = \mu_{\alpha}^{\mathrm{M}}[\overline{\mu}_{\alpha}] + \mu_{\alpha}^{\mathrm{S}}, \tag{13b}$$

where

$$\varphi^{\mathrm{M}}[\overline{\varphi}](\overline{\boldsymbol{x}}; \boldsymbol{x}, t) := \overline{\varphi}(\overline{\boldsymbol{x}}, t) + \overline{\boldsymbol{g}}^{\varphi}[\overline{\varphi}](\overline{\boldsymbol{x}}, t) \cdot [\boldsymbol{x} - \overline{\boldsymbol{x}}], \quad \overline{\boldsymbol{g}}^{\varphi} := \boldsymbol{\nabla} \overline{\varphi}, \tag{14a}$$

$$\mu_{\alpha}^{\mathrm{M}}[\overline{\mu}_{\alpha}](\overline{\boldsymbol{x}}; \boldsymbol{x}, t) := \overline{\mu}_{\alpha}(\overline{\boldsymbol{x}}, t) + \overline{\boldsymbol{g}}_{\alpha}^{\mu}[\overline{\mu}_{\alpha}](\overline{\boldsymbol{x}}, t) \cdot [\boldsymbol{x} - \overline{\boldsymbol{x}}], \quad \overline{\boldsymbol{g}}_{\alpha}^{\mu} := \boldsymbol{\nabla} \overline{\mu}_{\alpha}, \tag{14b}$$

for $\alpha = 1, 2, \ldots, N$. This corresponds to the standard prolongation approach where the sub-scale fields φ and μ_{α} are decomposed into macro-scale parts, φ^{M} and $\mu_{\alpha}^{\mathrm{M}}$, and micro-scale/fluctuating parts, φ^{S} and $\mu_{\alpha}^{\mathrm{S}}$. Note that it is the homogenized fields $\overline{\varphi}(\overline{\boldsymbol{x}}, t)$ and $\overline{\mu}_{\alpha}(\overline{\boldsymbol{x}}, t)$ that are the smooth macro-scale solutions. The macro-scale parts φ^{M} and $\mu_{\alpha}^{\mathrm{M}}$ only exist in the RVE problem as a means to create the fully resolved sub-scale fields.

Upon employing these steps within the VCH framework, a two-scale model is deduced from the single-scale model. The reader is referred to [22] for the details on exploiting VCH to deduce the two-scale model.

As previously mentioned, the two-scale problem can be solved via the FE^2 method. The procedure requires that the macro-scale and the sub-scale RVE problem are solved in a nested fashion with information passing in both directions. Information of the macro-scale solution is sent to the sub-scale in a prolongation step and serves as the loading data to the RVE problem. After solving the RVE problem, effective properties and effective fluxes are computed and sent back to the macro-scale in a homogenization step. This process takes place in every quadrature point, at every timestep.

3.1 | Homogenized Macro-Scale Problem

Upon exploiting VCH, the homogenized macro-scale problem is deduced. At every time instance, the macro-scale problem is formulated as follows: Find $(\overline{\varphi}, \{\overline{\mu}_\alpha\}) \in \overline{\mathbb{P}} \times \{\overline{\mathbb{M}}_\alpha\}$ that solve

$$\int_\Omega \delta\overline{\varphi}\ \overline{\rho} + \boldsymbol{\nabla}\delta\overline{\varphi} \cdot \overline{\boldsymbol{\rho}}^{(2)} + \boldsymbol{\nabla}\delta\overline{\varphi} \cdot \overline{\boldsymbol{d}}\ \mathrm{d}\Omega = -\int_{\Gamma_{\mathrm{N}}^{(\varphi)}} \delta\overline{\varphi}\ \overline{d}^{\mathrm{p}}\ \mathrm{d}\Gamma \qquad \forall \delta\overline{\varphi} \in \overline{\mathbb{P}}^0, \tag{15a}$$

$$\int_\Omega \delta\overline{\mu}_\alpha\ \partial_{\mathrm{t}}\overline{c}_\alpha + \boldsymbol{\nabla}\delta\overline{\mu}_\alpha \cdot \partial_{\mathrm{t}}\overline{\boldsymbol{c}}_\alpha^{(2)} - \boldsymbol{\nabla}\delta\overline{\mu}_\alpha \cdot \overline{\boldsymbol{j}}_\alpha\ \mathrm{d}\Omega = -\int_{\overline{\Gamma}_{\mathrm{N},\alpha}^{(\mu)}} \delta\overline{\mu}_\alpha\ \overline{j}_\alpha^{\mathrm{p}}\ \mathrm{d}\Gamma \quad \forall \delta\overline{\mu}_\alpha \in \overline{\mathbb{M}}_\alpha^0, \tag{15b}$$

for $\alpha = 1, 2, \ldots, N$ together with the initial condition

$$\int_\Omega \delta\overline{\mu}_\alpha \overline{c}_\alpha(\boldsymbol{x}, 0) + \boldsymbol{\nabla}\delta\overline{\mu} \cdot \overline{\boldsymbol{c}}_\alpha^{(2)}(\boldsymbol{x}, 0)\ \mathrm{d}\Omega = \int_\Omega \delta\overline{\mu}_\alpha \overline{c}_{\alpha,0}(\boldsymbol{x}) + \boldsymbol{\nabla}\delta\overline{\mu}_\alpha \cdot \overline{\boldsymbol{c}}_{\alpha,0}^{(2)}(\boldsymbol{x})\ \mathrm{d}\Omega, \tag{16}$$

where $\overline{c}_{\alpha,0}(\boldsymbol{x})$ and $\overline{\boldsymbol{c}}_{\alpha,0}^{(2)}$ can be deduced from a resolved initial condition $c_\alpha(\boldsymbol{x}, 0)$. The variationally consistent macro-scale (homogenized) constitutive quantities are defined as

$$\overline{\boldsymbol{d}} = \langle \boldsymbol{d} \rangle_\square = -\langle \boldsymbol{\epsilon} \cdot \boldsymbol{\nabla}\varphi \rangle_\square, \tag{17a}$$

$$\overline{\rho} = \langle \rho \rangle_\square = \phi \left\langle \sum_{\alpha=1}^{N} z'_\alpha\ c_\alpha \right\rangle_{\square,\mathrm{E}}, \tag{17b}$$

$$\overline{\boldsymbol{\rho}}^{(2)} = \langle \rho\ [\boldsymbol{x} - \overline{\boldsymbol{x}}] \rangle_\square, \tag{17c}$$

$$\overline{\boldsymbol{j}}_\alpha = \phi \langle \boldsymbol{j}_\alpha \rangle_{\square,\mathrm{E}} = -\phi \left\langle \boldsymbol{M}_\alpha \cdot (\boldsymbol{\nabla}\mu_\alpha + z'_\alpha \boldsymbol{\nabla}\varphi) \right\rangle_{\square,\mathrm{E}}, \tag{17d}$$

$$\overline{c}_\alpha = \phi \langle c_\alpha \rangle_{\square,\mathrm{E}}, \tag{17e}$$

$$\overline{\boldsymbol{c}}_\alpha^{(2)} = \phi \left\langle c_\alpha\ [\boldsymbol{x} - \overline{\boldsymbol{x}}] \right\rangle_{\square,\mathrm{E}}, \tag{17f}$$

$$\overline{\boldsymbol{i}} = \sum_\alpha z'_\alpha \overline{\boldsymbol{j}}_\alpha. \tag{17g}$$

3.2 | Sub-Scale RVE Problem

Upon exploiting VCH, the sub-scale RVE problem is deduced. At every time instance and for a given history $\overline{\varphi}(t)$, $\overline{\boldsymbol{g}}^{\varphi}(t)$, $\overline{\mu}_\alpha(t)$, $\overline{\boldsymbol{g}}_\alpha^{\mu}(t)$, the space-variational RVE-problem is formulated as follows: Find $\varphi \in \mathbb{P}_\square$, $\{\mu_\alpha\}_{\alpha=1}^N \in \{\boldsymbol{M}_{\square,\alpha}\}_{\alpha=1}^N$, $\lambda^{(\varphi)} \in \mathbb{T}_\square^{(\varphi)}$, $\lambda_\alpha^{(\mu)} \in \mathbb{T}_\square^{(\mu)}$, $\hat{\lambda}^{(\varphi)} \in \mathbb{R}$, $\hat{\lambda}_\alpha^{(\mu)} \in \mathbb{R}$ that solve

$$\sum_{\alpha=1}^{N} m_{\square,\alpha}^{(\varphi)}(\mu_\alpha, \delta\varphi) - a_\square^{(\varphi)}(\varphi, \delta\varphi) - \left\langle \left\langle \lambda^{(\varphi)} [\![\delta\varphi]\!]_\square \right\rangle \right\rangle_\square - \hat{\lambda}^{(\varphi)} \langle \delta\varphi \rangle_\square = 0$$

$$\forall \delta\varphi \in \mathbb{P}_\square, \tag{18a}$$

$$-\left\langle \left\langle \delta\lambda^{(\varphi)} [\![\varphi]\!]_\square \right\rangle \right\rangle_\square = -\left\langle \left\langle \delta\lambda^{(\varphi)} [\![\boldsymbol{x}]\!]_\square \right\rangle \right\rangle_\square \cdot \overline{\boldsymbol{g}}^{\varphi}$$

$$\forall \delta\lambda^{(\varphi)} \in \mathbb{T}_\square^{(\varphi)}, \tag{18b}$$

$$- \langle \varphi \rangle_{\square} \delta \hat{\lambda}^{(\varphi)} = -\overline{\varphi}\ \delta \hat{\lambda}^{(\varphi)}$$

$$\forall \delta \hat{\lambda}^{(\varphi)} \in \mathbb{R}, \tag{18c}$$

$$m^{(\mu)}_{\square,\alpha}(\partial_t \mu_\alpha, \delta\mu_\alpha) + a^{(\mu)}_{\square,\alpha}(\mu_\alpha, \delta\mu_\alpha) + a^{(\mu\ \varphi)}_{\square,\alpha}(\varphi, \delta\mu_\alpha) + \phi \left\langle \left\langle \lambda^{(\mu)}_\alpha [\![\delta\mu_\alpha]\!]_{\square} \right\rangle \right\rangle_{\square,\mathrm{E}} - \hat{\lambda}^{(\mu)}_\alpha\ \phi \langle \delta\mu_\alpha \rangle_{\square,\mathrm{E}} = 0$$

$$\forall \delta\mu_\alpha \in \mathbb{M}_{\square,\alpha}, \tag{18d}$$

$$\phi \left\langle \left\langle \delta\lambda^{(\mu)}_\alpha [\![\mu_\alpha]\!]_{\square} \right\rangle \right\rangle_{\square,\mathrm{E}} = \phi \left\langle \left\langle \delta\lambda^{(\mu)}_\alpha\ [\![\boldsymbol{x}]\!]_{\square} \right\rangle \right\rangle_{\square,\mathrm{E}} \cdot \overline{\boldsymbol{g}}^{\mu}_\alpha$$

$$\forall \delta\lambda^{(\mu)}_\alpha \in \mathbb{T}^{(\mu)}_{\square}, \tag{18e}$$

$$- \ \phi \langle \mu_\alpha \rangle_{\square,\mathrm{E}}\ \delta\hat{\lambda}^{(\mu)}_\alpha = -\phi(\overline{\mu}_\alpha + \overline{\boldsymbol{g}}^{\mu}_\alpha \cdot [\overline{\boldsymbol{x}}_{\mathrm{E}} - \overline{\boldsymbol{x}}])\ \delta\hat{\lambda}^{(\mu)}_\alpha$$

$$\forall \delta\hat{\lambda}^{(\mu)}_\alpha \in \mathbb{R}, \tag{18f}$$

for $\alpha = 1, 2, \ldots, N$ and appropriately defined initial conditions. The pertinent RVE forms in Equation (18) are given as

$$m^{(\varphi)}_{\square,\alpha}(\mu_\alpha, \delta\varphi) := \frac{1}{|\Omega_{\square}|} \int_{\Omega_{\square}} z'_\alpha k_\alpha \mu_\alpha\ \delta\varphi\ \mathrm{d}\Omega, \tag{19a}$$

$$a^{(\varphi)}_{\square}(\varphi, \delta\varphi) := \frac{1}{|\Omega_{\square}|} \int_{\Omega_{\square}} \boldsymbol{\nabla}\delta\varphi \cdot \boldsymbol{\epsilon} \cdot \boldsymbol{\nabla}\varphi\ \mathrm{d}\Omega, \tag{19b}$$

$$m^{(\mu)}_{\square,\alpha}(\mu_\alpha, \delta\mu_\alpha) := \frac{1}{|\Omega_{\square}|} \int_{\Omega_{\square,\mathrm{E}}} \mu_\alpha k_\alpha\ \delta\mu_\alpha\ \mathrm{d}\Omega, \tag{19c}$$

$$a^{(\mu)}_{\square,\alpha}(\mu_\alpha, \delta\mu_\alpha) := \frac{1}{|\Omega_{\square}|} \int_{\Omega_{\square,\mathrm{E}}} \boldsymbol{\nabla}\delta\mu_\alpha \cdot \boldsymbol{M}_\alpha \cdot \boldsymbol{\nabla}\mu_\alpha\ \mathrm{d}\Omega, \tag{19d}$$

$$a^{(\mu,\varphi)}_{\square,\alpha}(\varphi, \delta\mu_\alpha) := \frac{1}{|\Omega_{\square}|} \int_{\Omega_{\square,\mathrm{E}}} \boldsymbol{\nabla}\delta\mu_\alpha \cdot \boldsymbol{M}_\alpha \cdot z'_\alpha \boldsymbol{\nabla}\varphi\ \mathrm{d}\Omega. \tag{19e}$$

The difference operator $[\![\bullet]\!]_{\square}(\boldsymbol{x}) := \bullet(\boldsymbol{x}) - \bullet(\boldsymbol{x}^-(\boldsymbol{x}))$ is introduced upon enforcing weakly periodic boundary conditions [40]. Here, $\boldsymbol{x} \in \Gamma^+_{\square}$ is an image point whereas $\boldsymbol{x}^-(\boldsymbol{x}) \in \Gamma^- = \Gamma_{\square} \setminus \Gamma^+_{\square}$ is the corresponding mirror point. The physical meaning of the RVE constraint equations, and exact definitions of the trial and test spaces are left out for brevity; see [22] for further information.

Remark: From Equation (18), we conclude that the quantities defined in Equation (17) are invariant to the prescribed value $\overline{\varphi}$.

4 | Spatial Numerical Model Reduction of the RVE Problem

In an FE^2 setup, numerical integration is carried out at macroscopic quadrature points. Only one sub-scale RVE computation per macroscopic quadrature point is needed. However, for complex 3D macro-scale domains, the number of quadrature points rapidly increases, thus requiring a large number of sub-scale RVE computations. Together with the fact that the sub-scale RVE itself might also be complex, the FE^2 procedure quickly becomes computationally infeasible. In the subsequent sections, we reduce the computational burden of the FE^2 scheme by exploiting NMR to construct a surrogate model that is trained via POD snapshots of the primary fields. In such a case, the computationally expensive transient RVE problem is replaced by a cheap surrogate model, which simply consists of a system of ODEs. This circumvents the need for performing expensive RVE computations at every macroscopic quadrature point for all time steps; instead, a reduced system consisting of ODEs is solved in each macroscopic quadrature point.

The procedure is split into two stages: The off-line stage, where the surrogate model is constructed prior to the solution of the macro-scale problem, and the on-line stage, where the surrogate model is used to solve the macro-scale problem efficiently.

4.1 | "Stationary" Fields

To utilize NMR for the purpose of solving the RVE problems efficiently, it is convenient to introduce the following decomposition

$$\varphi(\boldsymbol{x},t) = \varphi^{\text{stat}}(\boldsymbol{x},t) + \varphi^{\text{trans}}(\boldsymbol{x},t), \tag{20a}$$

$$\mu_\alpha(\boldsymbol{x},t) = \mu_\alpha^{\text{stat}}(\boldsymbol{x},t) + \mu_\alpha^{\text{trans}}(\boldsymbol{x},t), \tag{20b}$$

for $\alpha = 1, 2, \dots, N$. Here, "stat" means stationary and "trans" means transient. These notations refer to the steady-state response due to sustained loading and to the response that contains relaxation processes when the loading is applied quickly, as compared to the relaxation time, respectively.

The stationary problem can be formulated as: For a given load $\overline{\varphi}$, $\boldsymbol{\nabla}\overline{\varphi}$, $\{\overline{\mu}_\alpha\}_{\alpha=1}^N$, $\{\boldsymbol{\nabla}\overline{\mu}_\alpha\}_{\alpha=1}^N$ (for $\alpha = 1, 2, \dots, N$) at every time instance t, find the time-independent stationary parts $\varphi^{\text{stat}}(\boldsymbol{x}) \in \mathbb{P}_\square$, $\{\mu_\alpha^{\text{stat}}(\boldsymbol{x})\}_{\alpha=1}^N \in \{\mathbb{M}_{\square,\alpha}\}_{\alpha=1}^N$, $\lambda^{(\varphi)}(\boldsymbol{x}) \in \mathbb{T}_\square$, $\lambda_\alpha^{(\mu)}(\boldsymbol{x}) \in \mathbb{T}_\square$, $\hat{\lambda}^{(\varphi)} \in \mathbb{R}$, $\hat{\lambda}_\alpha^{(\mu)} \in \mathbb{R}$ that solve

$$\sum_{\alpha=1}^N m_{\square,\alpha}^{(\varphi)}(\mu_\alpha^{\text{stat}}, \delta\varphi) - a_\square^{(\varphi)}(\varphi^{\text{stat}}, \delta\varphi) - \left\langle \left\langle \lambda^{(\varphi)} \; [\![\delta\varphi]\!]_\square \right\rangle \right\rangle_\square - \hat{\lambda}^{(\varphi)} \langle \delta\varphi \rangle_\square = 0$$

$$\forall \delta\varphi \in \mathbb{P}_\square, \tag{21a}$$

$$- \left\langle \left\langle \delta\lambda^{(\varphi)} \; [\![\varphi^{\text{stat}}]\!]_\square \right\rangle \right\rangle_\square = -\left\langle \left\langle \delta\lambda^{(\varphi)} [\![\boldsymbol{x}]\!]_\square \right\rangle \right\rangle_\square \cdot \overline{\boldsymbol{g}}^{\varphi}$$

$$\forall \delta\lambda^{(\varphi)} \in \mathbb{T}_\square^{(\varphi)}, \tag{21b}$$

$$- \left\langle \varphi^{\text{stat}} \right\rangle_\square \delta\hat{\lambda}^{(\varphi)} = -\overline{\varphi} \; \delta\hat{\lambda}^{(\varphi)}$$

$$\forall \delta\hat{\lambda}^{(\varphi)} \in \mathbb{R}, \tag{21c}$$

$$a_{\square,\alpha}^{(\mu)}(\mu_\alpha^{\text{stat}}, \delta\mu_\alpha) + a_{\square,\alpha}^{(\mu\ \varphi)}(\varphi^{\text{stat}}, \delta\mu_\alpha) + \phi \left\langle \left\langle \lambda_\alpha^{(\mu)} \; [\![\delta\mu_\alpha]\!]_\square \right\rangle \right\rangle_{\square,\text{E}} - \hat{\lambda}_\alpha^{(\mu)} \; \phi \langle \delta\mu_\alpha \rangle_{\square,\text{E}} = 0$$

$$\forall \delta\mu_\alpha \in \mathbb{M}_{\square,\alpha}, \tag{21d}$$

$$\phi \left\langle \left\langle \delta\lambda_\alpha^{(\mu)} \; [\![\mu_\alpha^{\text{stat}}]\!]_\square \right\rangle \right\rangle_{\square,\text{E}} = \phi \left\langle \left\langle \delta\lambda_\alpha^{(\mu)} \; [\![\boldsymbol{x}]\!]_\square \right\rangle \right\rangle_{\square,\text{E}} \cdot \overline{\boldsymbol{g}}_\alpha^{\mu}$$

$$\forall \delta\lambda_\alpha^{(\mu)} \in \mathbb{T}_\square^{(\mu)}, \tag{21e}$$

$$- \; \phi \left\langle \mu_\alpha^{\text{stat}} \right\rangle_{\square,\text{E}} \delta\hat{\lambda}_\alpha^{(\mu)} = -\phi(\overline{\mu}_\alpha + \overline{\boldsymbol{g}}_\alpha^{\mu} \cdot [\overline{\boldsymbol{x}}_\text{E} - \overline{\boldsymbol{x}}]) \; \delta\hat{\lambda}_\alpha^{(\mu)}$$

$$\forall \delta\hat{\lambda}_\alpha^{(\mu)} \in \mathbb{R}. \tag{21f}$$

Due to linearity, the time-dependent "stationary" parts $\bullet^{\text{stat}}(\boldsymbol{x},t)$ from Equation (21) can be decomposed into linear combinations that depend explicitly on the macroscopic loading histories

$$\varphi^{\text{stat}}(\boldsymbol{x},t) = \overline{\varphi}(t) + \boldsymbol{\varphi}_{\overline{g}^{\varphi}}(\boldsymbol{x}) \cdot \overline{\boldsymbol{g}}^{\varphi}(t) + \sum_{\alpha=1}^N \left(\varphi_{\overline{\mu}_\alpha}(\boldsymbol{x}) \overline{\mu}_\alpha(t) + \boldsymbol{\varphi}_{\overline{g}_\alpha^{\mu}}(\boldsymbol{x}) \cdot \overline{\boldsymbol{g}}_\alpha^{\mu}(t) \right), \tag{22a}$$

$$\mu_\alpha^{\text{stat}}(\boldsymbol{x},t) = \boldsymbol{\mu}_{\alpha,\overline{g}^{\varphi}}(\boldsymbol{x}) \cdot \overline{\boldsymbol{g}}^{\varphi}(t) + \sum_{\beta=1}^N \left(\mu_{\alpha,\overline{\mu}_\beta}(\boldsymbol{x}) \overline{\mu}_\beta(t) + \boldsymbol{\mu}_{\alpha,\overline{g}_\beta^{\mu}}(\boldsymbol{x}) \cdot \overline{\boldsymbol{g}}_\beta^{\mu}(t) \right), \tag{22b}$$

for $\alpha = 1, 2, \dots, N$. Each sensitivity field $[\boldsymbol{\varphi}_{\overline{g}^{\varphi}}, \varphi_{\overline{\mu}_\alpha}, \boldsymbol{\varphi}_{\overline{g}_\alpha^{\mu}}, \mu_{\alpha,\overline{\varphi}}, \boldsymbol{\mu}_{\alpha,\overline{g}^{\varphi}}, \mu_{\alpha,\overline{\mu}_\beta}, \boldsymbol{\mu}_{\alpha,\overline{g}_\beta^{\mu}}]$ is given by each corresponding time-independent unit sensitivity problem, see appendix in previous work [22]. Here, we made explicitly use of the trivial solution (sensitivity) $\varphi^{\text{stat}}(\boldsymbol{x}) = \overline{\varphi}$, $\mu_\alpha^{\text{stat}} = 0$, for $\alpha = 1, \dots, N$, for the case $\overline{\boldsymbol{g}}^{\varphi} = \overline{\boldsymbol{g}}_\alpha^{\mu} = \overline{\mu}_\alpha = 0$. Note that the stationary parts are effortlessly computed given that the macro-scale loading histories are known and that relevant sensitivity fields are pre-computed.

Next, we turn to solving the transient part of the solution by using substitution in the original equation (18). First, following the linearity and time-transience of Equations (18a–18c), we see that we can (formally) compute $\varphi^{\text{trans}}\{\{\mu_\alpha\}_{\alpha=1}^N\} = \varphi^{\text{trans}} \in \mathbb{P}_0$ together with Lagrange multipliers $(\hat{\lambda}^{\varphi}, \lambda^{\varphi}) \in \mathbb{R} \times \mathbb{P}_\square^{(\varphi)}$ such that

$$- a_\square^{(\varphi)}(\varphi, \delta\varphi) - \left\langle \left\langle \lambda^{(\varphi)} \; [\![\delta\varphi]\!]_\square \right\rangle \right\rangle_\square - \hat{\lambda}^{(\varphi)} \; \langle \delta\varphi \rangle_\square = -\sum_\alpha m_{\square,\alpha}^{(\varphi)}(\mu_\alpha^{\text{trans}}, \delta\varphi)$$

$$\forall \delta\varphi \in \mathbb{P}_\square, \tag{23a}$$

$$-\left\langle\left\langle \delta\lambda^{(\varphi)}\ [\![\varphi_\alpha]\!]_\square\right\rangle\right\rangle_\square = 0$$
$$\forall \delta\lambda^{(\varphi)} \in \mathbb{T}^{(\varphi)}_\square, \tag{23b}$$
$$-\delta\hat{\lambda}^{(\varphi)}\ \langle\varphi_a\rangle_\square = 0$$
$$\forall \delta\hat{\lambda}^{(\varphi)} \in \mathbb{R}. \tag{23c}$$

This problem follows directly by insertion of $\varphi = \varphi^{\text{stat}} + \varphi^{\text{trans}}$ and $\mu_\alpha = \mu^{\text{stat}}_\alpha + \mu^{\text{trans}}_\alpha$, while utilizing the relation in Equations (21a–21c). However, as a consequence of the split, we note that the value for the Lagrange multipliers in Equation (23) will in general not coincide with those in Equation (18).

Furthermore, we note that for a high dimension of $\{\mathbb{M}_{\square,\alpha}\}_{\alpha=1}^N$, or even worse, for the continuous case, the computation of $\varphi^{\text{trans}}\{\{\mu^{\text{trans}}_\alpha\}_{\alpha=1}^N\}$ is intractable in practice. However, as part of the reduced order model presented in Section 4.2, this limitation will be alleviated by introducing low-dimensional approximation spaces $\mathbb{M}_{\square,R,\alpha}$.

Assuming that we have the implicit relations $\varphi^{\text{trans}}\{\{\mu^{\text{trans}}_\alpha\}_{\alpha=1}^N\}$ at hand, we can solve for the transient parts μ^{trans}_a together with the Lagrange multipliers such that

$$m^{(\mu)}_{\square,\alpha}(\partial_t\mu^{\text{trans}}_\alpha, \delta\mu_\alpha) + a^{(\mu)}_{\square,\alpha}(\mu^{\text{trans}}_\alpha, \delta\mu_\alpha) + a^{(\mu\varphi)}_{\square,\alpha}(\varphi\{\{\mu^{\text{trans}}_\beta\}_{\alpha=1}^N\}, \delta\mu_\alpha)$$
$$+\phi\left\langle\left\langle \lambda^{(\mu)}_\alpha\ [\![\delta\mu_\alpha]\!]_\square\right\rangle\right\rangle_{\square,\text{E}} - \hat{\lambda}^{(\mu)}_\alpha\ \phi\langle\delta\mu_\alpha\rangle_{\square,\text{E}} = -m^{(\mu)}_{\square,\alpha}(\partial_t\mu^{\text{stat}}_\alpha, \delta\mu_\alpha)$$
$$\forall \delta\mu_\alpha \in \mathbb{M}_{\square,\alpha}, \tag{24a}$$
$$\phi\left\langle\left\langle \delta\lambda^{(\mu)}_\alpha\ [\![\mu^{\text{trans}}_\alpha]\!]_\square\right\rangle\right\rangle_{\square,\text{E}} = 0$$
$$\forall \delta\lambda^{(\mu)}_\alpha \in \mathbb{T}^{(\mu)}_\square, \tag{24b}$$
$$-\delta\hat{\lambda}^{(\mu)}_\alpha\ \phi\left\langle\mu^{\text{trans}}_\alpha\right\rangle_{\square,\text{E}} = 0$$
$$\forall \delta\hat{\lambda}^{(\mu)}_\alpha \in \mathbb{R}. \tag{24c}$$

Again, we remark that the Lagrange multipliers will in general not coincide with those in Equation (18).

In what follows, we shall introduce a reduced order approximation $\mu^{\text{trans}} \approx \mu^{\text{trans}}_R$. This will allow for (i) the explicit computation of the low dimensional mapping $\varphi\{\{\mu^{\text{trans}}_{\alpha,R}\}_{\alpha=1}^N\}$ from Equation (23), and (ii) Galerkin scheme for the reduced problem corresponding to (24).

4.2 | Generation of Basis for the Chemical Potential

The core of the surrogate model is the adoption of a reduced basis for the chemical potential field. We introduce the low dimensional spaces $\mathbb{M}_{\square,R,\alpha} = \text{span}\{\hat{\mu}_{\alpha,a}\}_{a=1}^{M_{R,\alpha}}$ and seek approximation of the transient fields on the form

$$\mu^{\text{trans}}_\alpha(\boldsymbol{x}, t) \approx \mu^{\text{trans}}_{\alpha,R}(\boldsymbol{x}, t) := \sum_{a=1}^{M_{R,\alpha}} \hat{\mu}_{\alpha,a}(\boldsymbol{x})\xi^{(\mu)}_{\alpha,a}(t) \in \mathbb{M}_{\square,R,\alpha}. \tag{25}$$

Here, $\{\hat{\mu}_{\alpha,a}\}_{a=1}^{M_{R,\alpha}}$ are a set of suitable basis functions for species α, and $M_{R,\alpha}$ is the number of these modes (typically much smaller than the dimension of the underlying FE-discretization).

As a first step, full (FE) simulations of Equations (18a–18f) for selected time histories $(\overline{\boldsymbol{g}}_\phi, \overline{\mu}_a, \overline{\boldsymbol{g}}_\mu)$ are carried out. These simulations are referred to as training simulations. Extracting spatial snapshots $\mu^{\text{trans}}_\alpha = \mu_\alpha - \mu^{\text{stat}}$ at selected time instances[2] $(a = 1, ..., S)$ from these simulations, we use Proper Orthogonal Decomposition (POD) to extract the most important modes and use them as a basis.

The chemical potential modes $\hat{\mu}_{\alpha,a}$ are obtained upon performing POD on the snapshot correlation matrices for all chemical species $\alpha = 1, 2, \ldots, N$. The snapshot correlation matrix is defined as follows

$$(\underline{G}_\alpha)_{ab} = \langle\mu^{\text{trans}}_{\alpha,a}(\boldsymbol{x})\ \mu^{\text{trans}}_{\alpha,b}(\boldsymbol{x})\rangle_\square, \quad a, b = 1, 2, ..., S. \tag{26}$$

Here, $\mu_{\alpha,a}^{\text{trans}}(\boldsymbol{x})$ corresponds to one of the S snapshots that are directly sampled from the transient solution $\mu_{\alpha}^{\text{trans}}(\boldsymbol{x},t)$. In the next step, the snapshot correlation matrices are used to solve the eigenvalue problem

$$((G_\alpha)_{ab} - \lambda\ \delta_{ab})\ \upsilon_{\alpha,b} = 0, \tag{27}$$

whereby the identified (orthonormal) eigenpairs $(\underline{\upsilon}_{\alpha}^{(a)}, \lambda_{\alpha}^{(a)})$, $a = 1, ..., S$, and the chemical potential snapshots $\mu_{\alpha,k}^{\text{trans}}(\boldsymbol{x})$ are used to compute the chemical potential modes as follows

$$\hat{\mu}_{\alpha,a}(\boldsymbol{x}) = \sum_{k=1}^{S} \left(\underline{\upsilon}_{\alpha}^{(a)}\right)_k\ \mu_{\alpha,k}^{\text{trans}}(\boldsymbol{x}). \tag{28}$$

Here, the entries in $\left(\underline{\upsilon}_{\alpha}^{(a)}\right)_k$ take the role of mixture coefficients in a linear combination of all transient snapshots to form each mode. By construction, the resulting chemical potential modes are orthogonal in a way such that

$$\langle \hat{\mu}_{\alpha,a}(\boldsymbol{x})\ \hat{\mu}_{\alpha,b}(\boldsymbol{x})\rangle_{\square} = \begin{cases} \lambda_{\alpha}^{(a)}, & \text{if } a = b, \\ 0, & \text{otherwise.} \end{cases} \tag{29}$$

To construct the reduced basis, we truncate the $M_{R,\alpha}$ modes with the highest eigenvalues $\lambda_{\alpha}^{(1)}, \lambda_{\alpha}^{(2)}, ..., \lambda_{\alpha}^{(M_{R,\alpha})}$.

4.3 | Identification of Modes for the Electric Potential

In the spirit of the Nonuniform Transformation Field Analysis (NTFA) [26], we shall now compute the pertinent modes for the electric potential. Using the fact that (23) is time invariant and linear, we may express

$$\varphi^{\text{trans}}\{\{\mu_{\alpha,R}^{\text{trans}}\}\} = \sum_{\alpha=1}^{N}\sum_{a=1}^{M_{R,\alpha}} \hat{\varphi}_{\alpha,a}(\boldsymbol{x})\xi_{\alpha,a}(t) \tag{30}$$

where the modes $\hat{\varphi}_{\alpha,a} \in \mathbb{P}_{\square}$ together with Lagrange multipliers $\lambda^{(\varphi)}, \overline{\lambda}^{(\varphi)} \in \mathbb{T}_{\square}^{(\varphi)} \times \mathbb{R}$ are solved such that

$$-a^{(\varphi)}(\hat{\varphi}_{\alpha,a}, \delta\varphi) - \left\langle\left\langle \lambda^{(\varphi)}\ [\![\delta\varphi]\!]\right\rangle\right\rangle_{\square} - \hat{\lambda}^{(\varphi)}\langle\delta\varphi\rangle_{\square} = -m_{\square,\alpha}^{(\varphi)}(\hat{\mu}_{\alpha,a}, \delta\varphi) \qquad \forall\delta\varphi \in \mathbb{P}_{\square}, \tag{31a}$$

$$-\left\langle\left\langle \delta\lambda^{(\varphi)}\ [\![\hat{\varphi}_{\alpha,a}]\!]\right\rangle\right\rangle_{\square} = 0 \qquad \forall\delta\lambda^{(\varphi)} \in \mathbb{T}_{\square}^{(\varphi)}, \tag{31b}$$

$$-\left\langle\hat{\varphi}_{\alpha,a}\right\rangle_{\square}\delta\hat{\lambda}^{(\varphi)} = 0 \qquad \forall\delta\hat{\lambda}^{(\varphi)} \in \mathbb{R}, \tag{31c}$$

for $a = 1, 2, \ldots, M_{R,\alpha}$ and $\alpha = 1, 2, \ldots, N$. Again, we note that the Lagrange multipliers will in general not coincide with those in Equation (18). Hence, the reduced approximation

$$\varphi_R(\boldsymbol{x},t) = \varphi^{\text{stat}}(\boldsymbol{x},t) + \sum_{\alpha}\sum_{a}\hat{\varphi}_{\alpha,a}\xi_{\alpha,a}(t), \tag{32a}$$

$$\mu_{\alpha,R}(\boldsymbol{x},t) = \mu_{\alpha}^{\text{stat}}(\boldsymbol{x},t) + \sum_{a}\hat{\mu}_{\alpha,a}\xi_{\alpha,a}(t), \quad \alpha = 1, ..., N, \tag{32b}$$

will satisfy Equations (18a–18c) exactly (up to the chosen FE-discretization).

4.4 | Establishing the Surrogate Model

The next step is to insert the appropriate NMR-approximations into the transient problem and choosing test functions according to $\delta\mu_{\alpha} = \hat{\mu}_{\alpha,a}$ in Equation (24a), $\delta\lambda_{\alpha}^{(\mu)} = \lambda_{\alpha,a}^{(\mu)}$ in Equation (24b) and $\delta\hat{\lambda}_{\alpha}^{(\mu)} = \hat{\lambda}_{\alpha,a}^{(\mu)}$ in Equation (24c):

$$\sum_{b=1}^{M_{R,\alpha}} m_{\square,\alpha}^{(\mu)}(\hat{\mu}_{\alpha,b}, \hat{\mu}_{\alpha,a})\dot{\xi}_{\alpha,b}^{(\mu)} + \sum_{b=1}^{M_{R,\alpha}} a_{\square_{\alpha}}^{(\mu)}(\hat{\mu}_{\alpha,b}, \hat{\mu}_{\alpha,a})\xi_{\alpha,b}^{(\mu)} + \sum_{\beta=1}^{N}\left(\sum_{b=1}^{M_{R,\alpha}} a_{\square,\alpha}^{(\mu\varphi)}(\hat{\varphi}_{\beta,b}, \hat{\mu}_{\alpha,a})\xi_{\beta,b}^{(\mu)}\right)$$
$$+\sum_{b=1}^{M_{R,\alpha}}\phi\left\langle\left\langle \lambda_{\alpha,b}^{(\mu)}\ [\![\hat{\mu}_{\alpha,a}]\!]\right\rangle\right\rangle_{\square,\text{E}}\xi_{\alpha,b}^{(\mu)} - \sum_{b=1}^{M_{R,\alpha}}\hat{\lambda}_{\alpha,b}^{(\mu)}\phi\left\langle\hat{\mu}_{\alpha,a}\right\rangle_{\square,\text{E}}\xi_{\alpha,b}^{(\mu)} = -m_{\square}^{(\mu)}(\partial_t\mu_{\alpha}^{\text{stat}}, \hat{\mu}_{\alpha,a}), \tag{33a}$$

$$\sum_{b=1}^{M_{R,\alpha}} \phi \left\langle \left\langle \lambda_{\alpha,b}^{(\mu)} \, [\![\hat{\mu}_{\alpha,a}]\!] \right\rangle \right\rangle_{\square,\mathrm{E}} \xi_{\alpha,b}^{(\mu)} = 0, \tag{33b}$$

$$- \sum_{b=1}^{M_{R,\alpha}} \hat{\lambda}_{\alpha,b}^{(\mu)} \phi \left\langle \hat{\mu}_{\alpha,a} \right\rangle_{\square,\mathrm{E}} \xi_{\alpha,b}^{(\mu)} = 0, \tag{33c}$$

for test functions $a = 1, 2, ..., M_{R,\alpha}$ and $\alpha = 1, 2, \dots, N$. Here, it is clear that (33b) and (33c) can be eliminated upon insertion into (33a).

As a final step, the stationary part $\mu_\alpha^{\mathrm{stat}}$ is decomposed according to (20) and the system of equations takes the following form

$$\begin{aligned} &\sum_{b=1}^{M_{R,\alpha}} m_{\square,\alpha}^{(\mu)}(\hat{\mu}_{\alpha,b}, \hat{\mu}_{\alpha,a}) \dot{\xi}_{\alpha,b}^{(\mu)} + \sum_{b=1}^{M_{R,\alpha}} a_{\square_\alpha}^{(\mu)}(\hat{\mu}_{\alpha,b}, \hat{\mu}_{\alpha,a}) \xi_{\alpha,b}^{(\mu)} + \sum_{\beta=1}^{N} \left(\sum_{b=1}^{M_{R,\alpha}} a_{\square,\alpha}^{(\mu\varphi)}(\hat{\varphi}_{\beta,b}, \hat{\mu}_{\alpha,a}) \xi_{\beta,b}^{(\mu)} \right) \\ &= -m_{\square,\alpha}^{(\mu)}(\mu_{\alpha,\overline{\varphi}}, \hat{\mu}_{\alpha,a}) \, \dot{\overline{\varphi}}(t) - m_{\square,\alpha}^{(\mu)}(\boldsymbol{\mu}_{\alpha,\overline{g}^\varphi}, \hat{\mu}_{\alpha,a}) \cdot \dot{\overline{\boldsymbol{g}}}^{\varphi}(t) - \sum_{\beta=1}^{N} m_{\square,\alpha}^{(\mu)}(\mu_{\alpha,\overline{\mu}_\beta}, \hat{\mu}_{\alpha,a}) \, \dot{\overline{\mu}}_\beta(t) - \sum_{\beta=1}^{N} m_{\square,\alpha}^{(\mu)}(\boldsymbol{\mu}_{\alpha,\overline{g}_\beta^\mu}, \hat{\mu}_{\alpha,a}) \cdot \dot{\overline{\boldsymbol{g}}}_\beta^{\mu}(t), \end{aligned} \tag{34}$$

for test functions $a = 1, 2, ..., M_{R,\alpha}$ and $\alpha = 1, 2, \dots, N$. For an arbitrary number of species α, the explicit format becomes as follows

$$\underline{\underline{M}}_{\alpha,\alpha} \, \underline{\dot{\xi}}_\alpha + \underline{\underline{K}}_{\alpha,\alpha} \, \underline{\xi}_\alpha + \sum_{\beta=1}^{N} \underline{\underline{K}}_{\alpha,\beta} \, \underline{\xi}_\beta = \underline{f}_{\alpha,\overline{\varphi}} \, \dot{\overline{\varphi}}(t) + \underline{\underline{f}}_{\alpha,\overline{g}^\varphi} \cdot \dot{\overline{\boldsymbol{g}}}^{\varphi}(t) + \sum_{\beta=1}^{N} \underline{f}_{\alpha,\overline{\mu}_\beta} \, \dot{\overline{\mu}}_\beta(t) + \sum_{\beta=1}^{N} \underline{\underline{f}}_{\alpha,\overline{g}_\beta^\mu} \cdot \dot{\overline{\boldsymbol{g}}}_\beta^{\mu}(t). \tag{35}$$

It is convenient to condense (35) into the following abbreviated matrix form

$$\underline{\underline{M}} \, \underline{\dot{\xi}} + \underline{\underline{K}} \, \underline{\xi} = \underline{f}, \tag{36}$$

with $\underline{\xi} = [\underline{\xi}_{\alpha_1}^{(\mu)}, \, \underline{\xi}_{\alpha_2}^{(\mu)}, \, \cdots, \, \underline{\xi}_{\alpha_N}^{(\mu)}]^T$ and $\underline{f} = [\underline{f}_{\alpha_1}, \, \underline{f}_{\alpha_2}, \, \cdots, \, \underline{f}_{\alpha_N}]^T$. For $\alpha = 1, 2, \dots, N$, the matrix entries are defined as

$$\left(\underline{\underline{M}}_{\alpha\alpha} \right)_{ab} = M_{\square,\alpha}(\hat{\mu}_{\alpha,b}, \hat{\mu}_{\alpha,a}), \tag{37a}$$

$$\left(\underline{\underline{K}}_{\alpha\alpha} \right)_{ab} = a_{\square,\alpha}^{(\mu)}(\hat{\mu}_{\alpha,b}, \hat{\mu}_{\alpha,a}) + a_{\square,\alpha}^{(\mu\varphi)}(\hat{\varphi}_{\alpha,b}, \hat{\mu}_{\alpha,a}), \tag{37b}$$

$$\left(\underline{\underline{K}}_{\alpha\beta} \right)_{ab} = a_{\square,\alpha}^{(\mu\varphi)}(\hat{\varphi}_{\beta,b}, \hat{\mu}_{\alpha,a}), \text{ where } \alpha \neq \beta. \tag{37c}$$

Moreover, the RHS of (36), representing the macroscopic loading, is given as

$$\left(\underline{f}_\alpha \right)_a = -m_{\square,\alpha}^{(\mu)}(\boldsymbol{\mu}_{\alpha,\overline{g}^\varphi}, \hat{\mu}_{\alpha,a}) \cdot \dot{\overline{\boldsymbol{g}}}^{\varphi}(t) - \sum_{\beta=1}^{N} m_{\square,\alpha}^{(\mu)}(\mu_{\alpha,\overline{\mu}_\beta}, \hat{\mu}_{\alpha,a}) \, \dot{\overline{\mu}}_\beta(t) - \sum_{\beta=1}^{N} m_{\square,\alpha}^{(\mu)}(\boldsymbol{\mu}_{\alpha,\overline{g}_\beta^\mu}, \hat{\mu}_{\alpha,a}) \cdot \dot{\overline{\boldsymbol{g}}}_\beta^{\mu}(t). \tag{38}$$

In the present paper, only Li-ions (Li^+) and the corresponding anion (X^-) are considered; the explicit format becomes as follows

$$\begin{aligned} \underline{\underline{M}}_{\mathrm{Li,Li}} \, \underline{\dot{\xi}}_{\mathrm{Li}} + \underline{\underline{K}}_{\mathrm{Li,Li}} \, \underline{\xi}_{\mathrm{Li}} + \underline{\underline{K}}_{\mathrm{Li,X}} \, \underline{\xi}_{\mathrm{X}} &= \underline{f}_{\mathrm{Li},\overline{\varphi}} \, \dot{\overline{\varphi}}(t) + \underline{\underline{f}}_{\mathrm{Li},\overline{g}^\varphi} \cdot \underline{\dot{g}}^{\varphi}(t) \\ &+ \underline{f}_{\mathrm{Li},\overline{\mu}_{\mathrm{Li}}} \, \dot{\overline{\mu}}_{\mathrm{Li}}(t) + \underline{\underline{f}}_{\mathrm{Li},\overline{g}_{\mathrm{Li}}^\mu} \cdot \underline{\dot{g}}_{\mathrm{Li}}^{\mu}(t) \\ &+ \underline{f}_{\mathrm{Li},\overline{\mu}_{\mathrm{X}}} \, \dot{\overline{\mu}}_{\mathrm{X}}(t) + \underline{\underline{f}}_{\mathrm{Li},\overline{g}_{\mathrm{X}}^\mu} \cdot \underline{\dot{g}}_{\mathrm{X}}^{\mu}(t), \end{aligned} \tag{39a}$$

$$\begin{aligned} \underline{\underline{M}}_{\mathrm{X,X}} \, \underline{\dot{\xi}}_{\mathrm{X}} + \underline{\underline{K}}_{\mathrm{X,Li}} \, \underline{\xi}_{\mathrm{Li}} + \underline{\underline{K}}_{\mathrm{X,X}} \, \underline{\xi}_{\mathrm{X}} &= \underline{f}_{\mathrm{X},\overline{\varphi}} \, \dot{\overline{\varphi}}(t) + \underline{\underline{f}}_{\mathrm{X},\overline{g}^\varphi} \cdot \underline{\dot{g}}^{\varphi}(t) \\ &+ \underline{f}_{\mathrm{X},\overline{\mu}_{\mathrm{Li}}} \, \dot{\overline{\mu}}_{\mathrm{Li}}(t) + \underline{\underline{f}}_{\mathrm{X},\overline{g}_{\mathrm{Li}}^\mu} \cdot \underline{\dot{g}}_{\mathrm{Li}}^{\mu}(t) \\ &+ \underline{f}_{\mathrm{X},\overline{\mu}_{\mathrm{X}}} \, \dot{\overline{\mu}}_{\mathrm{X}}(t) + \underline{\underline{f}}_{\mathrm{X},\overline{g}_{\mathrm{X}}^\mu} \cdot \underline{\dot{g}}_{\mathrm{X}}^{\mu}(t). \end{aligned} \tag{39b}$$

In matrix form, it becomes

$$\begin{bmatrix} \underline{\underline{M}}_{\mathrm{Li,Li}} & \underline{\underline{0}} \\ \underline{\underline{0}} & \underline{\underline{M}}_{\mathrm{X,X}} \end{bmatrix} \begin{bmatrix} \dot{\underline{\xi}}_{\mathrm{Li}} \\ \dot{\underline{\xi}}_{\mathrm{X}} \end{bmatrix} + \begin{bmatrix} \underline{\underline{K}}_{\mathrm{Li,Li}} & \underline{\underline{K}}_{\mathrm{Li,X}} \\ \underline{\underline{K}}_{\mathrm{X,Li}} & \underline{\underline{K}}_{\mathrm{X,X}} \end{bmatrix} \begin{bmatrix} \underline{\xi}_{\mathrm{Li}} \\ \underline{\xi}_{\mathrm{X}} \end{bmatrix} = \begin{bmatrix} \underline{f}_{\mathrm{Li}} \\ \underline{f}_{\mathrm{X}} \end{bmatrix}. \tag{40}$$

Here, note that the surrogate model does not track material state variables in the classical sense, as they are not included in the constitutive laws of the RVE problem. However, since the surrogate model takes the form of a system of coupled ODEs, it requires initial conditions and needs to keep track of the histories of the activity coefficients. Hence, the activity coefficients represent the internal variables in a macroscopic sense [33, 34]. Equation (36) is the set of evolutions of those internal variables representing the sub-scale transport properties.

With the surrogate model in hand, we can now define the approximate effective fluxes directly as a function of activity coefficients. This is achieved upon inserting $\varphi = \varphi^{\mathrm{stat}} + \varphi^{\mathrm{trans}}$ and $\mu_\alpha = \mu_\alpha^{\mathrm{stat}} + \mu_\alpha^{\mathrm{trans}}$ from Equations (22) and (25). Repeating this for all the effective fluxes defined in Equation (17) results in the following relations that can be used in the NMR-FE2 framework

$$\begin{aligned}
\overline{\boldsymbol{d}} \approx & -\left\langle \boldsymbol{\epsilon}[\boldsymbol{\nabla} \otimes \boldsymbol{\varphi}_{\overline{g}^{\varphi}}] \right\rangle_{\square} \cdot \overline{\boldsymbol{g}}^{\varphi} - \sum_{\alpha=1}^{N} \left(\left\langle \boldsymbol{\epsilon} \boldsymbol{\nabla} \varphi_{\overline{\mu}_\alpha} \right\rangle_{\square} \overline{\mu}_\alpha + \left\langle \boldsymbol{\epsilon} \boldsymbol{\nabla} \otimes \boldsymbol{\varphi}_{\overline{g}^{\mu}_\alpha} \right\rangle_{\square} \cdot \overline{\boldsymbol{g}}^{\mu}_\alpha \right) \\
& - \sum_{\alpha}^{N} \left[\sum_{a}^{M_{R,\alpha}} \left\langle \boldsymbol{\epsilon} \boldsymbol{\nabla} \hat{\varphi}_{\alpha,a} \right\rangle_{\square} \xi^{(\mu)}_{\alpha,a} \right], \qquad (41a) \\
\overline{\boldsymbol{j}}_\alpha \approx & -\phi \left\langle \boldsymbol{M}_\alpha \cdot (\boldsymbol{\nabla} \otimes \boldsymbol{\mu}_{\alpha,\overline{g}^{\varphi}} + z'_\alpha \boldsymbol{\nabla} \otimes \boldsymbol{\varphi}_{\overline{g}^{\varphi}}) \right\rangle_{\square,\mathrm{E}} \cdot \overline{\boldsymbol{g}}^{\varphi} \\
& - \sum_{\beta=1}^{N} \left(\phi \left\langle \boldsymbol{M}_\alpha \cdot (\boldsymbol{\nabla} \mu_{\alpha,\overline{\mu}_\beta} + z'_\alpha \boldsymbol{\nabla} \varphi_{\overline{\mu}_\beta}) \right\rangle_{\square,\mathrm{E}} \overline{\mu}_\beta + \phi \left\langle \boldsymbol{M}_\alpha \cdot (\boldsymbol{\nabla} \otimes \boldsymbol{\mu}_{\alpha,\overline{g}^{\mu}_\beta} + z'_\alpha \boldsymbol{\nabla} \otimes \boldsymbol{\varphi}_{\overline{g}^{\mu}_\beta}) \right\rangle_{\square,\mathrm{E}} \cdot \overline{\boldsymbol{g}}^{\mu}_\beta \right) \\
& - \sum_{a}^{M_{R,\alpha}} \phi \left\langle \boldsymbol{M}_\alpha \boldsymbol{\nabla} \hat{\mu}_{\alpha,a} \right\rangle_{\square,\mathrm{E}} \xi^{(\mu)}_{\alpha,a} - \sum_{\beta}^{N} \left[\sum_{a}^{M_{R,\alpha}} \phi \left\langle \boldsymbol{M}_\alpha z'_\alpha \boldsymbol{\nabla} \hat{\varphi}_{\beta,a} \right\rangle_{\square,\mathrm{E}} \xi^{(\mu)}_{\beta,a} \right], \qquad (41b) \\
\overline{c}_\alpha \approx & \phi \left\langle k_\alpha \boldsymbol{\mu}_{\alpha,\overline{g}^{\varphi}} \right\rangle_{\square,\mathrm{E}} \cdot \overline{\boldsymbol{g}}^{\varphi} + \sum_{\beta}^{N} \left(\phi \left\langle k_\alpha \mu_{\alpha,\overline{\mu}_\beta} \right\rangle_{\square,\mathrm{E}} \overline{\mu}_\beta + \phi \left\langle k_\alpha \boldsymbol{\mu}_{\alpha,\overline{g}^{\mu}_\beta} \right\rangle_{\square,\mathrm{E}} \cdot \overline{\boldsymbol{g}}^{\mu}_\beta \right) \\
& + \sum_{a}^{M_{R,\alpha}} \phi \left\langle k_\alpha \hat{\mu}_{\alpha,a} \right\rangle_{\square,\mathrm{E}} \xi^{(\mu)}_{\alpha,a} + \phi \left\langle c_{\alpha,0} \right\rangle_{\square,\mathrm{E}}, \qquad (41c) \\
\overline{\boldsymbol{c}}^{(2)}_\alpha \approx & \phi \left\langle k_\alpha \boldsymbol{\mu}_{\alpha,\overline{g}^{\varphi}} [\boldsymbol{x} - \overline{\boldsymbol{x}}] \right\rangle_{\square,\mathrm{E}} \cdot \overline{\boldsymbol{g}}^{\varphi} + \sum_{\beta}^{N} \left(\phi \left\langle k_\alpha \mu_{\alpha,\overline{\mu}_\beta} [\boldsymbol{x} - \overline{\boldsymbol{x}}] \right\rangle_{\square,\mathrm{E}} \overline{\mu}_\beta + \phi \left\langle k_\alpha \boldsymbol{\mu}_{\alpha,\overline{g}^{\mu}_\beta} [\boldsymbol{x} - \overline{\boldsymbol{x}}] \right\rangle_{\square,\mathrm{E}} \cdot \overline{\boldsymbol{g}}^{\mu}_\beta \right) \\
& + \sum_{a}^{M_{R,\alpha}} \phi \left\langle k_\alpha \hat{\mu}_{\alpha,a} [\boldsymbol{x} - \overline{\boldsymbol{x}}] \right\rangle_{\square,\mathrm{E}} \xi^{(\mu)}_{\alpha,a} + \phi \left\langle c_{\alpha,0} [\boldsymbol{x} - \overline{\boldsymbol{x}}] \right\rangle_{\square,\mathrm{E}}, \qquad (41d)
\end{aligned}$$

whereby the remaining effective fluxes are trivially derived as

$$\overline{\rho} = \sum_{\alpha=1}^{N} z'_\alpha \overline{c}_\alpha, \tag{42a}$$

$$\overline{\boldsymbol{\rho}}^{(2)} = \sum_{\alpha=1}^{N} z'_\alpha \overline{\boldsymbol{c}}^{(2)}_\alpha, \tag{42b}$$

$$\overline{\boldsymbol{i}} = \sum_{\alpha=1}^{N} z'_\alpha \overline{\boldsymbol{j}}_\alpha. \tag{42c}$$

5 | Numerical Examples of the Surrogate Model

The surrogate model performance is evaluated and compared against a reference solution obtained by solving a DNS problem. The training data for NMR is obtained upon solving the RVE problem for various loading cases. The considered

numerical example for the RVE problem allows for ionic transport exclusively in the electrolyte domain. All simulations are performed using COMSOL Multiphysics©.

5.1 | RVE With Ionic Transport Exclusively in the Electrolyte Domain

In the considered numerical example, the computational domain of the RVE consists of 1158 elements, which corresponds to 6154 degrees of freedom when using quadratic shape functions for all fields. The linear-transient training simulations start at $1 \cdot 10^{-13}$ s and end at $1 \cdot 10^{0}$ s across 50 time steps that are spaced out evenly on a logarithmic scale, resulting in, on average, 3.8 steps per decade.

The RVE loading cases take the form of prescribed macro-scale fields and gradients (componentwise, one by one) via prolongation[3]; i.e., $\overline{\varphi}$, $\boldsymbol{\nabla}\overline{\varphi}$, $\overline{\mu}_\alpha$ and $\boldsymbol{\nabla}\overline{\mu}_\alpha$. Upon limiting the numerical examples to the two ionic species Li^+ and X^-, the number of unit RVE loading cases for training corresponds to 9 in 2D. The macro-scale fields and gradients are prescribed in analogy to a stress relaxation test by ramping them up and keeping them constant upon reaching the given magnitude. The ramping signal is smooth and cosine-based; see Figure 2 for the ramping signal that mimics a (discrete) step input.

Being able to design a systematic training strategy, consisting of a step input in every component of all primary fields and gradients, is one of the main appeals of this framework. Due to the problem being of a linear-transient type, the superposition principle applies, and the individual training loads can form arbitrary linear combinations. In other words, this strategy limits the number of training simulations to only a few cases. It would be unreasonable to train on all combinations and shapes of input signals, as solving such a large number of RVE problems in the offline stage would be computationally intractable. Furthermore, training only for certain multi-load cases can cause the surrogate model to struggle with generalization if the model overfits. The idea behind using step inputs in the training simulations is to simultaneously excite all the relaxation modes of the system, since a step input contains a wide spectrum of frequencies [33]. Here, the relaxation properties of the system come from the fact that the transient problem allows for the redistribution of ionic species within the RVE.

For each RVE problem that is solved, snapshots of the transient part of RVE primary fields $\mu_\alpha^{\text{trans}}$ are collected into a snapshot matrix. See Figure 3 for examples of snapshots. Although not used in the POD procedure, the electric potential at the selected time instances is shown for illustration purposes. A snapshot correlation matrix is computed based on the snapshot matrix, whereby an eigendecomposition provides the coefficients necessary to form POD modes as a linear combination of the transient snapshots. Examples of the chemical potential modes and the computed electric potential modes (see Section 4.3) are shown in Figure 4.

The identified POD modes are used to construct a surrogate model consisting of a system of first-order ODEs according to (35). A necessary, albeit not sufficient, condition for a properly trained surrogate model is that it must be able to reproduce the training data, given that the same loading data is used as in the training simulations. The surrogate model validation based on reproduction of training responses can be seen in Figure 5. Note that the effective fluxes are reproduced properly. Additionally, the accuracy of the reproduced effective fluxes increases with the number of modes that are included in the training of the surrogate model.

In the next step, the surrogate model is used and properly validated in a two-scale simulation by comparing its results with a separate DNS simulation that is used as a reference solution. Instead of performing the two-scale simulation based on FE^2, the surrogate model replaces the boundary value problems pertaining to the 2D RVE in the sub-scale denoted

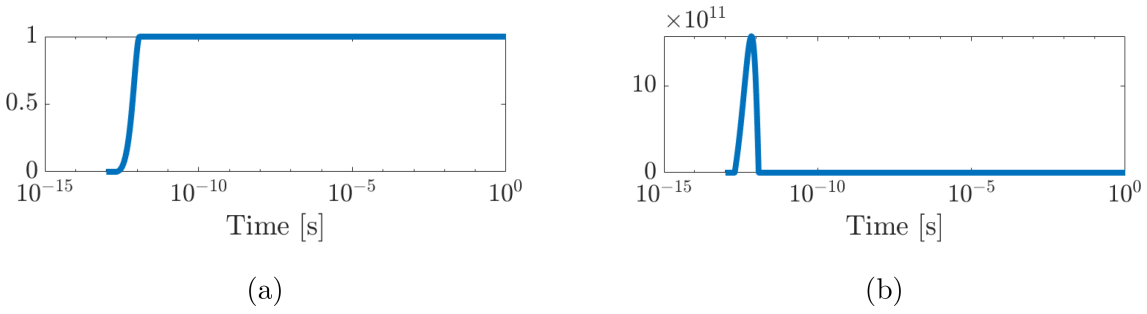

FIGURE 2 | RVE ramp signal shown in (a) and the corresponding ramp rate in (b).

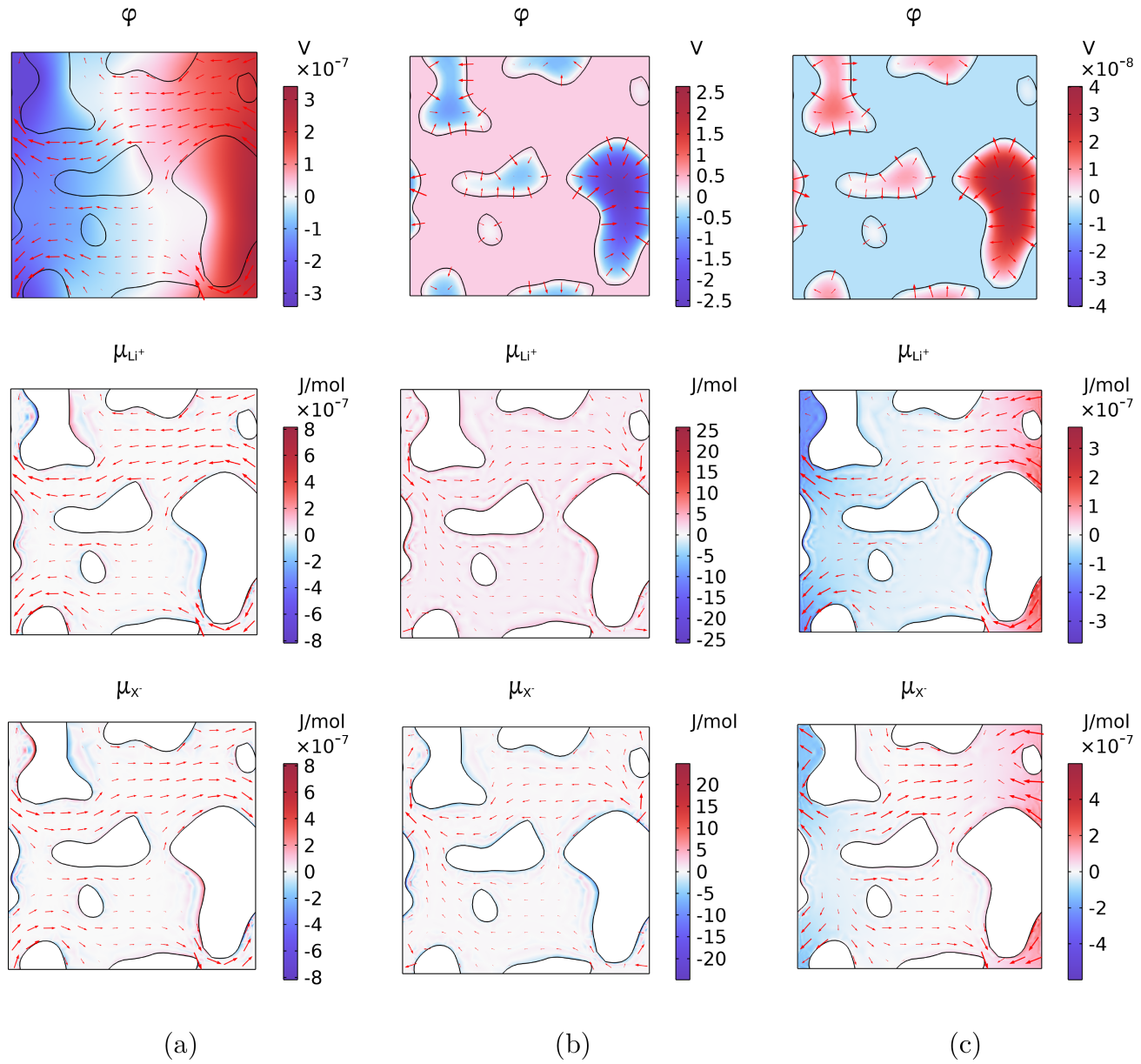

FIGURE 3 | Snapshots taken from $t = 1.1482 \cdot 10^{-5}$ s; 2D RVE with macroscopic loading in column (a) $\nabla\varphi$ (x-component), column (b) $\overline{\mu}_{\mathrm{Li}^+}$, and column (c) $\nabla\mu_{\mathrm{Li}^+}$ (x-component). The red arrows represent $\boldsymbol{d}$, $\boldsymbol{j}_{\mathrm{Li}^+}$ and $\boldsymbol{j}_{\mathrm{X}^-}$ in the plots for φ, μ_{Li^+} and μ_{X^-}, respectively.

reduced FE^2 (entitled NMR-FE2 in the plots). In the validation, both the DNS and reduced FE^2 are subjected to the same prescribed boundary conditions; different electric potential values are prescribed along the left and right boundaries, which results in an electric field between the boundaries in the x-direction. Furthermore, the chemical potential of Li^+ is set to zero on both the left and right boundaries to enable a non-zero stationary ionic flux through these boundaries. Consequently, the Dirichlet boundary conditions on μ_{Li^+} function as an infinite sink and source. In contrast, the chemical potential of X^- is subject to zero flux boundary conditions. Lastly, periodic boundary conditions are applied to all fields at both the top and bottom boundaries. See Figure 6 for a schematic of the validation procedure. It can be seen in Figure 7 that the macro-scale fluxes, taken from the center of the computational domain, are accurately predicted by the reduced FE^2 scheme compared to the DNS reference.

5.2 | NMR Training Strategies

The standard method to train an NMR surrogate model is to compute a single correlation matrix containing all snapshots at once. This method is henceforth denoted POD-1. However, it is important to consider that the chemical potential fields and their magnitudes might look significantly different depending on the loading case during training. Therefore,

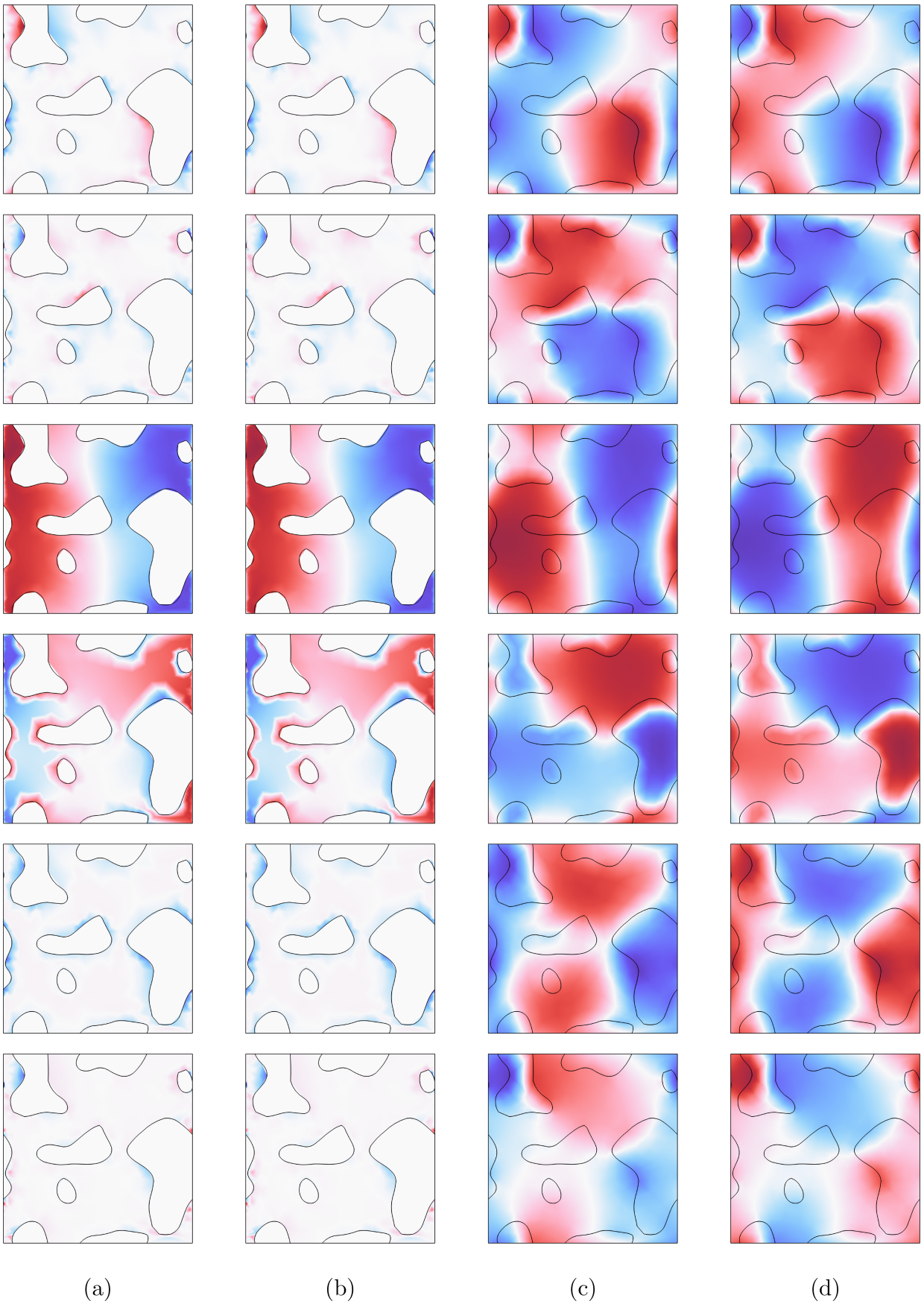

FIGURE 4 | POD modes grouped columnwise; (a) $\hat{\mu}_{Li^+}$, (b) $\hat{\mu}_{X^-}$, (c) $\hat{\varphi}_{Li^+}$, and (d) $\hat{\varphi}_{X^-}$.

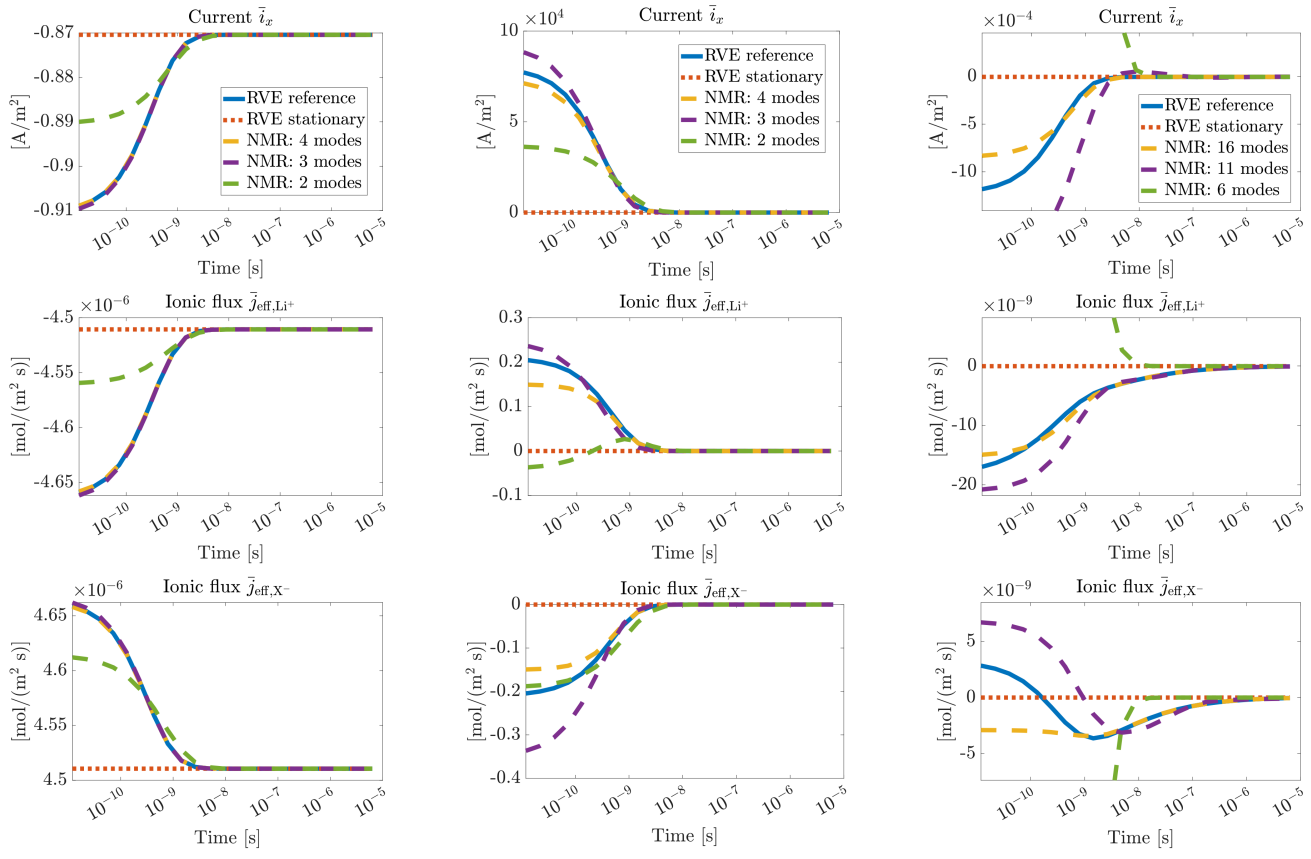

FIGURE 5 | NMR model reproducing the training data with macroscopic loading in (a) $\nabla\overline{\varphi}$ (x-component), (b) $\overline{\mu}_{\text{Li}^+}$, and (c) $\nabla\overline{\mu}_{\text{Li}^+}$ (x-component).

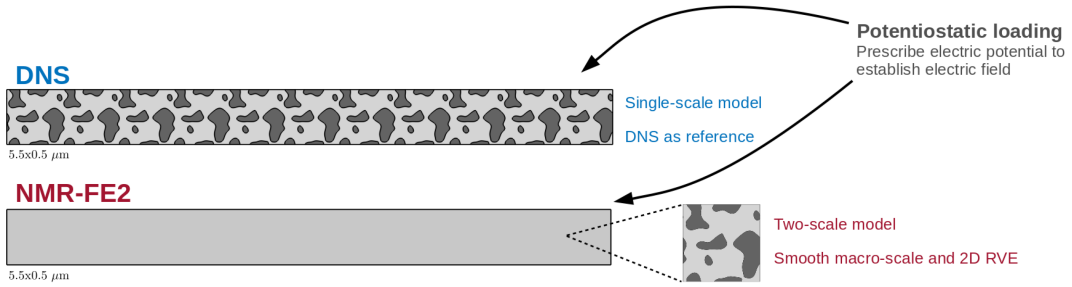

FIGURE 6 | Schematic of the validation procedure for the surrogate model.

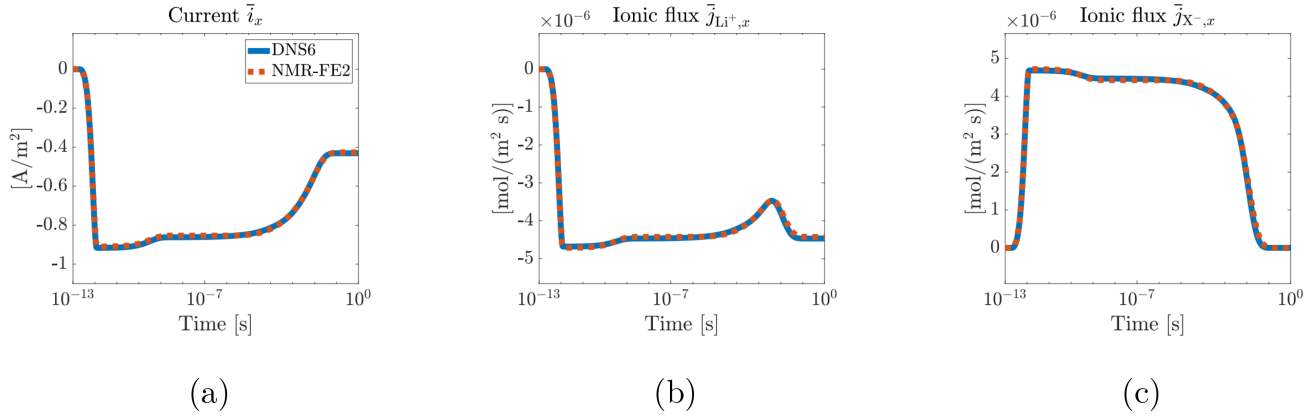

FIGURE 7 | Validation of reduced FE^2 against DNS solution; (a) current, (b) effective ionic flux Li$^+$, and (c) effective ionic flux X$^-$.

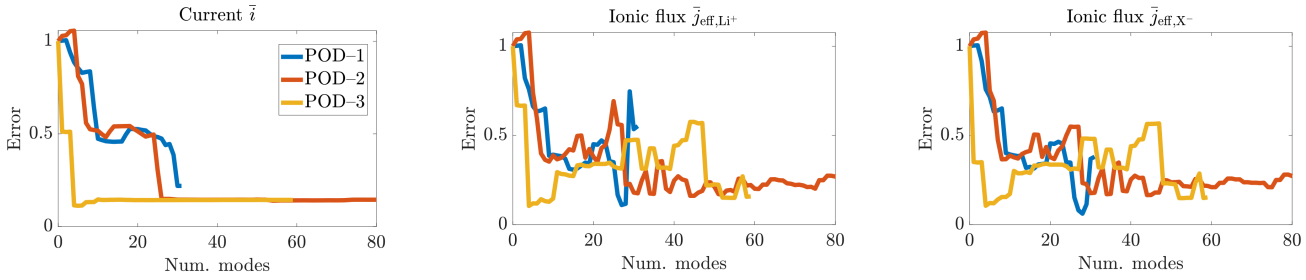

FIGURE 8 | Normalized RMS error of NMR predictions of a validation loading case; (a) current (in x-component), (b) ionic flux Li^+ (in x-component), and (c) ionic flux X^- (in x-component).

a viable method is to compute two different correlation matrices for the gradient- and non-gradient-based loading cases, respectively. This method is henceforth denoted POD-2; it consists of snapshots from loading cases in all primary fields in the first correlation matrix, while all snapshots from gradient-based loading cases belong to the second correlation matrix. In other words, the training data is split into

i. $\overline{\mu}_\alpha$,

ii. $\nabla\overline{\varphi}$ and $\nabla\overline{\mu}_\alpha$.

In the next step, a POD is performed on both correlation matrices, resulting in two sets of POD modes that are merged and used together in the surrogate model. Another viable method is to not only split the gradient- and non-gradient-based loading cases, but also consider that the loading cases might stem from different physics in multi-physics problems. This method will be denoted POD-3, as the split will be performed for

i. $\nabla\overline{\varphi}$,

ii. $\overline{\mu}_\alpha$,

iii. $\nabla\overline{\mu}_\alpha$.

for $\alpha = [\text{Li}^+, \text{X}^-]$This results in 3 sets of POD modes that are later merged and used together in the surrogate model.

In Figure 8, we study how the normalized RMS error of NMR predictions varies with the number of modes. Here, we use a validation loading case that has not been trained for. It is a multi-field loading case consisting of 6 simultaneous loading signals in x-direction in 2D; namely $\overline{\varphi}$, $\partial_x\overline{\varphi}$, $\overline{\mu}_{\text{Li}^+}$, $\partial_x\overline{\mu}_{\text{Li}^+}$, $\overline{\mu}_{\text{X}^-}$ and $\partial_x\overline{\mu}_{\text{X}^-}$. Consider a certain quantity of interest q, then the normalized root mean square (RMS) error is computed as

$$\text{Error} = \frac{\sqrt{\sum \left(q_{\text{NMR}} - q_{\text{ref}}\right)^2}}{\sqrt{\sum q_{\text{ref}}^2}}. \tag{43}$$

Figure 8 shows that the NMR error behaves differently depending on the quantity of interest. For the effective current $\bar{i}$, the error will, in general, decrease when more modes are added. However, for the effective ionic fluxes $\bar{j}_{\text{eff},\alpha}$, certain specific mode combinations provide significantly smaller error. It is also evident that POD-3 performs better than POD-1 and POD-2 in terms of accuracy for almost any given number of modes. Note that POD-2 and POD-3 also perform better in terms of computational cost; it is much more efficient to perform POD on multiple small correlation matrices, rather than using one single large correlation matrix.

One issue with the current training strategy is that there are a substantial number of modes that do not contribute to predicting the transient response, especially in view of the effective ionic fluxes. Instead, there exist a few critical modes that are responsible for predicting most of the transient part. Currently, the modes are selected in an order that is based on the magnitude of their corresponding eigenvalues; this method seems to work well only for the first few modes. Taking this into consideration, it means that the current NMR framework still has room for improvement; e.g., it would be much more appealing to adaptively pick out and train with only the best modes in view of error minimization.

TABLE 1 | Solution times in COMSOL Multiphysics of various RVE and NMR problems.

Model	Size		Wall-clock time [s]
RVE1	6154 dofs		27
RVE2	27,040 dofs		59
RVE3	68,916 dofs		172
NMR1	20 modes		3
NMR2	40 modes		6
NMR3	59 modes		13
NMR speed-up factors	**RVE1**	**RVE2**	**RVE3**
NMR1	9	19.7	57.3
NMR2	4.5	9.8	28.7
NMR3	2.1	4.5	13.2

5.3 | Computational Cost of NMR

In theory, the performance boost (in terms of code execution speed) from exploiting NMR in two-scale modeling can be arbitrarily high. Consider the case where the computational cost of solving an RVE problem is increased via mesh refinements; this does not automatically result in an increase in the computational cost of solving the surrogate model, since the number of modes might not necessarily increase. Consequently, while the computational effort of solving the RVE might be arbitrarily high, the effort of solving the surrogate model can stay relatively constant given that no new modes are added.

Table 1 shows the elapsed real time (wall-clock time) for solving RVE problems and evaluating surrogate models of various sizes. The RVE problems are once again driven by a multi-field (validation) loading case in x-direction in 2D, involving six simultaneous loading signals over 50 time steps, as in Section 5.2. These computations were performed in COMSOL Multiphysics version 6.0, on a Dell Latitude-7490 with the i7-8650U CPU (4 physical cores with a base speed frequency of 1.90 GHz each).

6 | Conclusions and Outlook

In this paper, we have developed a framework for exploiting NMR in a multi-physics two-scale simulation of linear-transient character. The NMR method is based on using POD to identify modes from training data, whereby the modes are used to establish a surrogate model that comprises a system of ODEs. The surrogate model is able to make accurate predictions, cf. the training results in Figure 5 and validation results in Figure 7. Exploiting NMR for the considered two-scale problem can result in a speed-up factor of up to 57 on a Dell Latitude-7490 with the i7-8650U CPU.

We also explored different training strategies; they are denoted POD-1, POD-2, and POD-3. It turns out that there are substantial benefits to splitting the training data into multiple categories, depending on whether the training data was generated using a gradient-based or a non-gradient-based loading condition. It was found that splitting the training data, and therefore performing multiple PODs, leads to higher accuracy on the NMR predictions and also decreases the computational cost of the offline training phase. However, this training strategy still has potential for significant improvements; the results in Figure 8 indicate that accurate NMR predictions are possible with even fewer modes, given that the mode selection is performed optimally.

In classical POD problems, dominant modes are typically identified based on the magnitude of the eigenvalues because they contribute most to accurately representing the system behavior. However, the challenges observed in this paper are related to the fact that the original problem is a coupled multi-physics system that requires training for multiple primary variables. In this case, it is not trivial to identify the optimal strategy for constructing the combined reduced POD basis. Since the quality of the reduced basis determines the accuracy of the NMR output, a promising direction for future work is to develop error estimators for predefined quantities of interest to adaptively identify the need for basis enrichment

via so-called "local modes", as inspired by, e.g., Borggaard et al. [41]. Additionally, the framework would benefit from an in-depth investigation into quantifying how well the surrogate model generalizes based on the chosen training set.

While numerical investigations in this paper are restricted to 2D microstructures, extension to 3D RVEs is straightforward, cf. Tu et al. 2023 [22]. Future work should generalize the approach for applications with transport in both solid and liquid phases, as well as interaction kinetics at the solid-fluid interface. This would allow for studying, e.g., electrode material.

One of the limitations of this framework is that the training phase is valid only for one type of RVE; hence, changing the RVE requires re-training of the surrogate model. There have been attempts at generalizing the geometric aspect of these types of frameworks, but it's still limited to linear re-scaling of simple features, such as, e.g., circles and ellipses.

For future work, the electro-chemical framework can be extended to non-dilute (concentrated) solutions by introducing the non-linear activity coefficient $\gamma = \gamma(c)$, which is suitably computed using, e.g., the extended Debye-Hückel equation or the Pitzer equations. The biggest challenge with non-linear constitutive relations is that a lot of the (computational) speed-up is lost, since we are now required to revisit every macroscopic quadrature point during the global iterations. In other words, the integration becomes a major contribution to the total computational cost. A viable strategy to tackle this issue is to consider the concept of hyperreduction, which relies on a reduced integration domain for resolving the non-linear constitutive equations. Since the integrations are not made over the entire domain, an extrapolation is later exploited over the full domain [42]. Another possibility is to consider the Discrete Empirical Interpolation Method (DEIM), which reduces the components of the global internal force vector to a set of reduction nodes; hence, the numerical integration is only performed in the quadrature points of the elements surrounding the selected reduction nodes [43].

The manufacturing process of the structural battery electrolyte is still being researched as it is one of the most complex, yet critical, parts of the structural battery. While it is possible to perform experimental validation, much work still remains to be done in this research topic, both experimentally and computationally. This paper only serves as a first building block, and a more in-depth and complete modeling approach will be needed to capture all the complex phenomena that might appear in the experiments.

Acknowledgments

This research was funded by the Swedish Research Council (VR) via the Grant Nos. 2017-05192, 2019-05080, and 2020-05057. Furthermore, funding was also received from the USAF EOARD (Award No. FA8655-21-1-7038). All are gratefully acknowledged.

Funding

This work was supported by Vetenskapsrådet (Grant Nos. 2017-05192, 2019-05080, and 2020-05057) and the USAF EOARD (Grant No. FA8655-21-1-7038).

Conflicts of Interest

The authors declare no conflicts of interest.

Data Availability Statement

The data that support the findings of this study are available from the corresponding author upon reasonable request.

Endnotes

[1] In literature, similar approaches are also referred to as Reduced Order Modeling (ROM) and Model Order Reduction (MOR).

[2] Here, each snapshot is indicated by a given time instance from one solution μ_α. In practice, the snapshots are typically extracted from different simulations.

[3] Note that the fields resulting from the loading case $\overline{\varphi}$ are stationary and uniform. Hence, this loading will be disregarded when analyzing the transient solutions using NMR.

References

1. N. Ihrner, W. Johannisson, F. Sieland, D. Zenkert, and M. Johansson, "Structural Lithium Ion Battery Electrolytes via Reaction Induced Phase-Separation," *Journal of Materials Chemistry A* 5, no. 48 (2017): 25652–25659.

2. L. M. Schneider, N. Ihrner, D. Zenkertand, and M. Johansson, "Bicontinuous Electrolytes via Thermally Initiated Polymerization for Structural Lithium Ion Batteries," *ACS Applied Energy Materials* 2 (2019): 4362–4369.

3. V. Tu, L. E. Asp, N. Shirshova, K. Larsson, R. Runesson, and R. Jänicke, "Performance of Bicontinuous Structural Electrolytes," *Multifunctional Materials* 3 (2020): 025001.

4. S. Duan, M. Cattaruzza, V. Tu, et al., "Three-Dimensional Reconstruction and Computational Analysis of a Structural Battery Composite Electrolyte," *Communications Materials* 4 (2023): 49.

5. L. E. Asp, M. Johansson, G. Lindbergh, J. Xu, and D. Zenkert, "Structural Battery Composites: A Review," *Functional Composites and Structures* 1 (2019): 042001.

6. N. Shirshova, P. Johansson, M. J. Marczewski, et al., "Polymerised High Internal Phase Ionic Liquid-In-Oil Emulsions as Potential Separators for Lithium Ion Batteries," *Journal of Materials Chemistry A* 1, no. 34 (2013): 9612–9619.

7. J. Newman and W. Tiedemann, "Porous-Electrode Theory With Battery Applications," *AICHE Journal* 21 (1975): 25–41.

8. M. Doyle, T. F. Fuller, and J. Newman, "Modeling of Galvanostatic Charge and Discharge of the Lithium/Polymer/Insertion Cell," *Journal of the Electrochemical Society* 140 (1993): 1526–1533.

9. M. Doyle and J. Newman, "The Use of Mathematical Modeling in the Design of Lithium/Polymer Battery Systems," *Electrochimica Acta* 40 (1995): 2191–2196, International Symposium on Polymer Electrolytes.

10. E. Samson, J. Marchand, J.-L. Robert, and J.-P. Bournazel, "Modelling Ion Diffusion Mechanisms in Porous Media," *International Journal for Numerical Methods in Engineering* 46 (1999): 2043–2060.

11. D. Danilov and P. Notten, "Mathematical Modelling of Ionic Transport in the Electrolyte of li Batteries," *Electrochimica Acta* 53 (2008): 5569–5578.

12. R. G. C. Edmund, J. F. Dickinson, and J. G. LimonPetersen, "The Electroneutrality Approximation in Electrochemistry," *Journal of Solid State Electrochemistry* 15 (2011): 1335–1345.

13. G. Bauer, V. Gravemeier, and W. A. Wall, "A Stabilized Finite Element Method for the Numerical Simulation of Multi-Ion Transport in Electrochemical Systems," *Computer Methods in Applied Mechanics and Engineering* 223-224 (2012): 199–210.

14. C. Miehe, J. Schröder, and J. Schotte, "Computational Homogenization Analysis in Finite Plasticity Simulation of Texture Development in Polycrystalline Materials," *Computer Methods in Applied Mechanics and Engineering* 171 (1999): 387–418.

15. M. Geers, V. Kouznetsova, and W. Brekelmans, "Multi-Scale Computational Homogenization: Trends and Challenges," *Journal of Computational and Applied Mathematics* 234 (2010): 2175–2182, Fourth International Conference on Advanced COmputational Methods in ENgineering (ACOMEN 2008).

16. I. Özdemir, W. Brekelmans, and M. Geers, "FE2 Computational Homogenization for the Thermo-Mechanical Analysis of Heterogeneous Solids," *Computer Methods in Applied Mechanics and Engineering* 198 (2008): 602–613.

17. J. Schröder and M.-A. Keip, "Two-Scale Homogenization of Electromechanically Coupled Boundary Value Problems: Consistent Linearization and Applications," *Computational Mechanics* 50 (2012): 229–244.

18. A. Javili, G. Chatzigeorgiou, and P. Steinmann, "Computational Homogenization in Magneto-Mechanics," *International Journal of Solids and Structures* 50 (2013): 4197–4216.

19. A. Salvadori, E. Bosco, and D. Grazioli, "A Computational Homogenization Approach for li-Ion Battery Cells: Part 1 Formulation," *Journal of the Mechanics and Physics of Solids* 65 (2014): 114–137.

20. A. Salvadori, D. Grazioli, and M. Geers, "Governing Equations for a Two-Scale Analysis of li-Ion Battery Cells," *International Journal of Solids and Structures* 59 (2015): 90–109.

21. A. Salvadori, D. Grazioli, M. Geers, D. Danilov, and P. Notten, "A Multiscale-Compatible Approach in Modeling Ionic Transport in the Electrolyte of (Lithium Ion) Batteries," *Journal of Power Sources* 293 (2015): 892–911.

22. V. Tu, F. Larsson, K. Runesson, and R. Jänicke, "Variationally Consistent Homogenization of Electrochemical Ion Transport in a Porous Structural Battery Electrolyte," *European Journal of Mechanics - A/Solids* 98 (2023): 104901.

23. C. Oskay and J. Fish, "Eigendeformation-Based Reduced Order Homogenization for Failure Analysis of Heterogeneous Materials," *Computer Methods in Applied Mechanics and Engineering* 196 (2007): 1216–1243.

24. G. J. Dvorak, "Transformation Field Analysis of Inelastic Composite Materials," *Proceedings of the Royal Society of London. Series A: Mathematical and Physical Sciences* 437 (1992): 311–327.

25. G. Dvorak, A. Wafa, and Y. BaheiElDin, "Implementation of the Transformation Field Analysis for Inelastic Composite Materials," *Computational Mechanics* 14 (1994): 201–228.

26. J. Michel and P. Suquet, "Nonuniform Transformation Field Analysis," *International Journal of Solids and Structures* 40 (2003): 6937–6955, Special Issue in Honor of George J. Dvorak.

27. J. Yvonnet and Q.-C. He, "The Reduced Model Multiscale Method (R3M) for the Non-Linear Homogenization of Hyperelastic Media at Finite Strains," *Journal of Computational Physics* 223 (2007): 341–368.

28. E. Monteiro, J. Yvonnet, and Q. He, "Computational Homogenization for Nonlinear Conduction in Heterogeneous Materials Using Model Reduction," *Computational Materials Science* 42 (2008): 704–712.

29. T. Guo, O. Rokoš, and K. Veroy, "Learning Constitutive Models From Microstructural Simulations via a Non-Intrusive Reduced Basis Method," *Computer Methods in Applied Mechanics and Engineering* 384 (2021): 113924.

30. S. Roussette, J. Michel, and P. Suquet, "Nonuniform Transformation Field Analysis of Elastic Viscoplastic Composites," *Composites Science and Technology* 69 (2009): 22–27, Mechanical Response of Fibre Reinforced Composites.

31. F. Fritzen and M. Leuschner, "Reduced Basis Hybrid Computational Homogenization Based on a Mixed Incremental Formulation," *Computer Methods in Applied Mechanics and Engineering* 260 (2013): 143–154.

32. F. Fritzen and T. Böhlke, "Reduced Basis Homogenization of Viscoelastic Composites," *Composites Science and Technology* 76 (2013): 84–91.

33. R. Jänicke, F. Larsson, K. Runesson, and H. Steeb, "Numerical Identification of a Viscoelastic Substitute Model for Heterogeneous Poroelastic Media by a Reduced Order Homogenization Approach," *Computer Methods in Applied Mechanics and Engineering* 298 (2016): 108–120.

34. R. Jänicke, F. Larsson, and K. Runesson, "A Poro-Viscoelastic Substitute Model of Fine-Scale Poroelasticity Obtained From Homogenization and Numerical Model Reduction," *Computational Mechanics* 65 (2020): 1063–1083.

35. F. Ekre, F. Larsson, K. Runesson, and R. Jänicke, "A Posteriori Error Estimation for Numerical Model Reduction in Computational Homogenization of Porous Media," *International Journal for Numerical Methods in Engineering* 121 (2020): 5350–5380.

36. F. Larsson, K. Runesson, and F. Su, "Variationally Consistent Computational Homogenization of Transient Heat Flow," *International Journal for Numerical Methods in Engineering* 81 (2010): 1659–1686.

37. J. Newman and N. P. Balsara, *Electrochemical Systems*, 4th ed. (John Wiley & Sons, 2021), 608.

38. P. W. Atkins, *Physical Chemistry*, 5th ed. (Oxford University Press, 1994).

39. L. Liu, A. Sridhar, M. Geers, and V. Kouznetsova, "Computational Homogenization of Locally Resonant Acoustic Metamaterial Panels Towards Enriched Continuum Beam/Shell Structures," *Computer Methods in Applied Mechanics and Engineering* 387 (2021): 114161.

40. K. Runesson, S. Saroukhani, and R. Vafadari, "Computational Homogenization Based on a Weak Format of Micro-Periodicity for RVE-Problems," *Computer Methods in Applied Mechanics and Engineering* 200 (2011): 11–26.

41. J. Borggaard, Z. Wang, and L. Zietsman, "A Goal-Oriented Reduced-Order Modeling Approach for Nonlinear Systems," *Computers & Mathematics With Applications* 71 (2016): 2155–2169, Proceedings of the conference on Advances in Scientific Computing and Applied Mathematics. A Special Issue in Honor of Max Gunzburger's 70th Birthday.

42. D. Ryckelynck, "Hyper-Reduction of Mechanical Models Involving Internal Variables," *International Journal for Numerical Methods in Engineering* 77 (2009): 75–89.

43. S. Chaturantabut and D. C. Sorensen, "Nonlinear Model Reduction via Discrete Empirical Interpolation," *SIAM Journal on Scientific Computing* 32 (2010): 2737–2764.